Quaternary Science Reviews 113 (2015) 93–111

Contents lists available at ScienceDirect

Quaternary Science Reviews

journal homepage: www.elsevier.com/locate/quascirev

Coastal evidence for Holocene subduction-zone earthquakes and tsunamis in central Chile

Tina Dura [a, c, d, *], Marco Cisternas [b], Benjamin P. Horton [c, d, e], Lisa L. Ely [f], Alan R. Nelson [g], Robert L. Wesson [g], Jessica E. Pilarczyk [c, d, e]

[a] Department of Earth and Environmental Science, The University of Pennsylvania, Philadelphia, PA, USA
[b] Escuela de Ciencias del Mar, Pontificia Universidad Católica de Valparaíso, Valparaíso, Chile
[c] Sea Level Research, Department of Marine and Coastal Science, Rutgers University, New Brunswick, NJ, USA
[d] Institute of Earth, Ocean, and Atmospheric Sciences, Rutgers University, New Brunswick, NJ, USA
[e] Earth Observatory of Singapore and Division of Earth Sciences, Nanyang Technological University, Singapore
[f] Department of Geological Sciences, Central Washington University, Ellensburg, WA, USA
[g] U.S. Geological Survey, Golden, CO, USA

ARTICLE INFO

Article history:
Received 31 May 2014
Received in revised form
25 September 2014
Accepted 17 October 2014
Available online 13 November 2014

Keywords:
Prehistoric earthquakes
Tsunami deposits
Diatom paleoecology
Coastal paleoseismology
Coastal hazards

ABSTRACT

The ~500-year historical record of seismicity along the central Chile coast (30–34°S) is characterized by a series of ~M 8.0–8.5 earthquakes followed by low tsunamis (<4 m) occurring on the megathrust about every 80 years. One exception is the AD 1730 great earthquake (M 9.0–9.5) and high tsunami (>10 m), but the frequency of such large events is unknown. We extend the seismic history of central Chile through a study of a lowland stratigraphic sequence along the metropolitan coast north of Valparaíso (33°S). At this site, higher relative sea level during the mid Holocene created a tidal marsh and the accommodation space necessary for sediment that preserves earthquake and tsunami evidence. Within this 2600-yr-long sequence, we traced six laterally continuous sand beds probably deposited by high tsunamis. Plant remains that underlie the sand beds were radiocarbon dated to 6200, 5600, 5000, 4400, 3800, and 3700 cal yr BP. Sediment properties and diatom assemblages of the sand beds—for example, anomalous marine planktonic diatoms and upward fining of silt-sized diatom valves—point to a marine sediment source and high-energy deposition. Grain-size analysis shows a strong similarity between inferred tsunami deposits and modern coastal sediment. Upward fining sequences characteristic of suspension deposition are present in five of the six sand beds. Despite the lack of significant lithologic changes between the sedimentary units under- and overlying tsunami deposits, we infer that the increase in freshwater siliceous microfossils in overlying units records coseismic uplift concurrent with the deposition of five of the sand beds. During our mid-Holocene window of evidence preservation, the mean recurrence interval of earthquakes and tsunamis is ~500 years. Our findings imply that the frequency of historical earthquakes in central Chile is not representative of the greatest earthquakes and tsunamis that the central Chilean subduction zone has produced.

1. Introduction

The most densely populated portion of the Chilean coast lies along the central Chilean subduction zone, a historically active segment of the megathrust between 30° and 34°S (Fig. 1; Lomnitz, 2004; Métois et al., 2012). Historical accounts from central Chile describe destructive earthquakes in AD 1575, 1580, 1647, 1730, 1822, 1906, and 1985 (Lomnitz, 1970, 2004; Cisternas et al., 2012). The consistent recurrence interval (~80 years; Comte et al., 1986; Barrientos, 2007) suggests the next large earthquake will not occur until the mid-21st century. But the 2004 Andaman-Aceh (Sumatra) and 2011 Tohoku-oki (Japan) multi-segment subduction-zone earthquakes and accompanying tsunamis highlight the risk of basing hazard assessment solely on well-documented historical events (Rhodes et al., 2006; Geller, 2011; Heki, 2011; Stein and Okal, 2011). The consistency of the historical recurrence interval in central Chile is misleading because rupture lengths and amounts of slip on the megathrust differ substantially among earthquakes (Fig. 1b; Moreno and Gibbons, 2007; Cisternas et al.,

* Corresponding author. Department of Earth and Environmental Science, The University of Pennsylvania, 240 S. 33rd St., Philadelphia, 19104, PA, USA. Tel.: +1 530 990 3468.
E-mail address: dura@sas.upenn.edu (T. Dura).

http://dx.doi.org/10.1016/j.quascirev.2014.10.015
0277-3791/

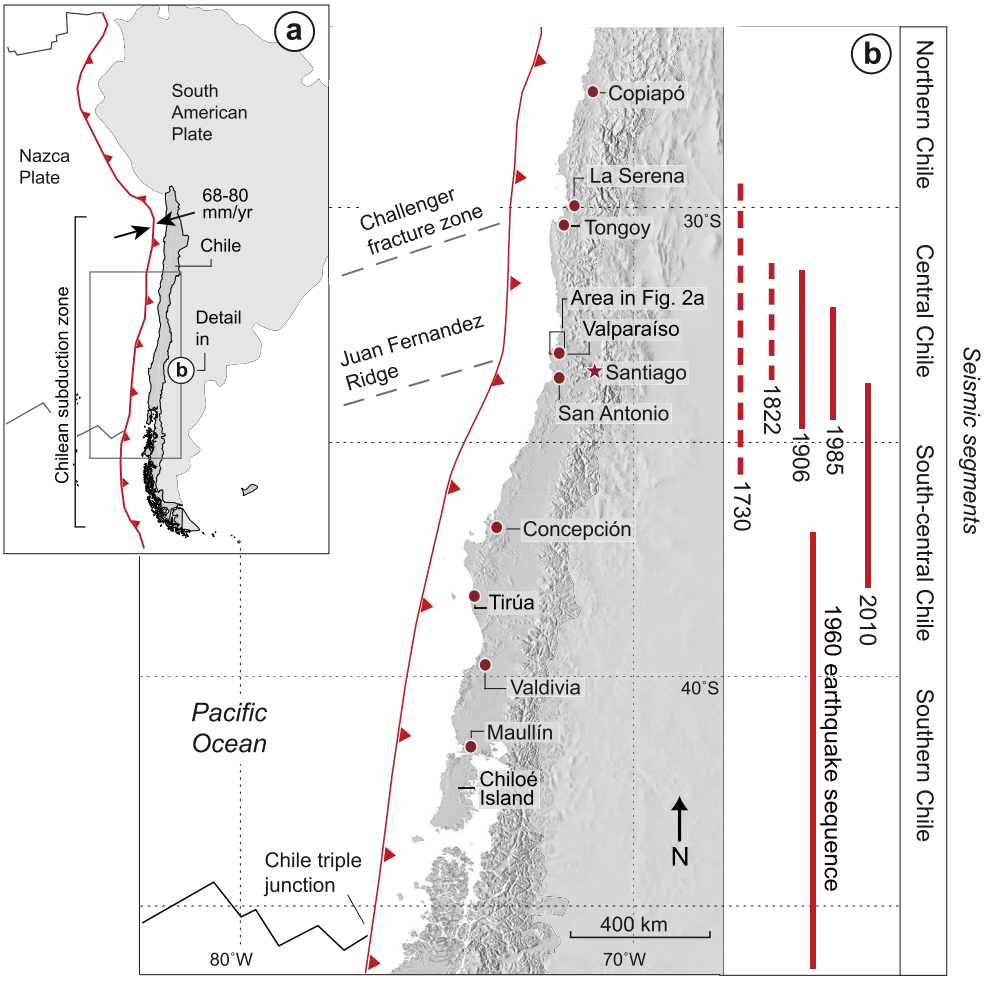

Fig. 1. Index maps. a) Plate-tectonic setting of Chile in western South America. b) Location of the study area in central Chile, seismic segments, main tectonic features, and estimated rupture lengths of the largest historical earthquakes in central Chile since 1730 compiled from Lomnitz (1970), Kelleher (1972), Comte et al. (1986), Beck et al. (1998), and Melnick et al. (2009). The 1960, 2010 ruptures are shown for comparison.

2012). The height of tsunamis accompanying historical earthquakes has also varied. The most recent and well-documented historical earthquakes in AD 1822, 1906 and 1985 were M 8.0–8.5 events that produced localized damage and relatively low tsunamis (<4 m). The AD 1730 earthquake, which is not as well documented because it occurred when the coastal population was sparse, caused widespread damage and produced a high tsunami on both the Chilean (Lomnitz, 1970; Udías et al., 2012) and Japanese coasts (Soloviev and Go, 1984). Based on the widespread tsunami, the 1730 earthquake was at least as large as the M_w 8.8 2010 Maule, Chile earthquake that devastated south-central Chile. However, such an earthquake has not recurred in the last ~300 years, and, thus, is not considered to be typical of the central Chilean subduction zone (Vigny et al., 2011). In order to better assess hazards along this segment of the subduction zone, we need to know how often 1730-style earthquakes and tsunamis have occurred. Such knowledge can only be gained by extending the record of earthquakes and tsunamis in central Chile back in time.

Stratigraphic evidence of great subduction-zone earthquakes, like that discovered in the tidal marshes of Chile (Atwater et al., 1992; Bartsch-Winkler and Schmoll, 1993; Cisternas et al., 2005; Nelson et al., 2009), Alaska (Ovenshine and Lawson, 1976; Combellick and Reger, 1994; Shennan and Hamilton, 2006), and the U.S. Pacific Northwest (Darienzo et al., 1994; Atwater and Hemphill-Haley, 1997; Nelson et al., 1998), can be used to develop histories of large earthquakes that extend over multiple earthquake cycles. Coseismic vertical deformation of the coastline may be recorded in coastal sedimentary sequences as a series of sudden

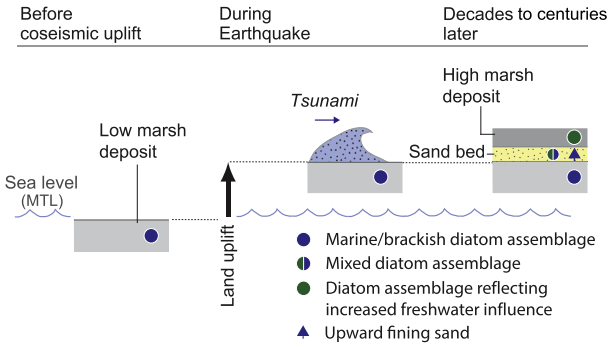

Fig. 2. Schematic drawing of coseismic uplift and tsunami inundation in central Chile (modified from Atwater and Hemphill-Haley, 1997).

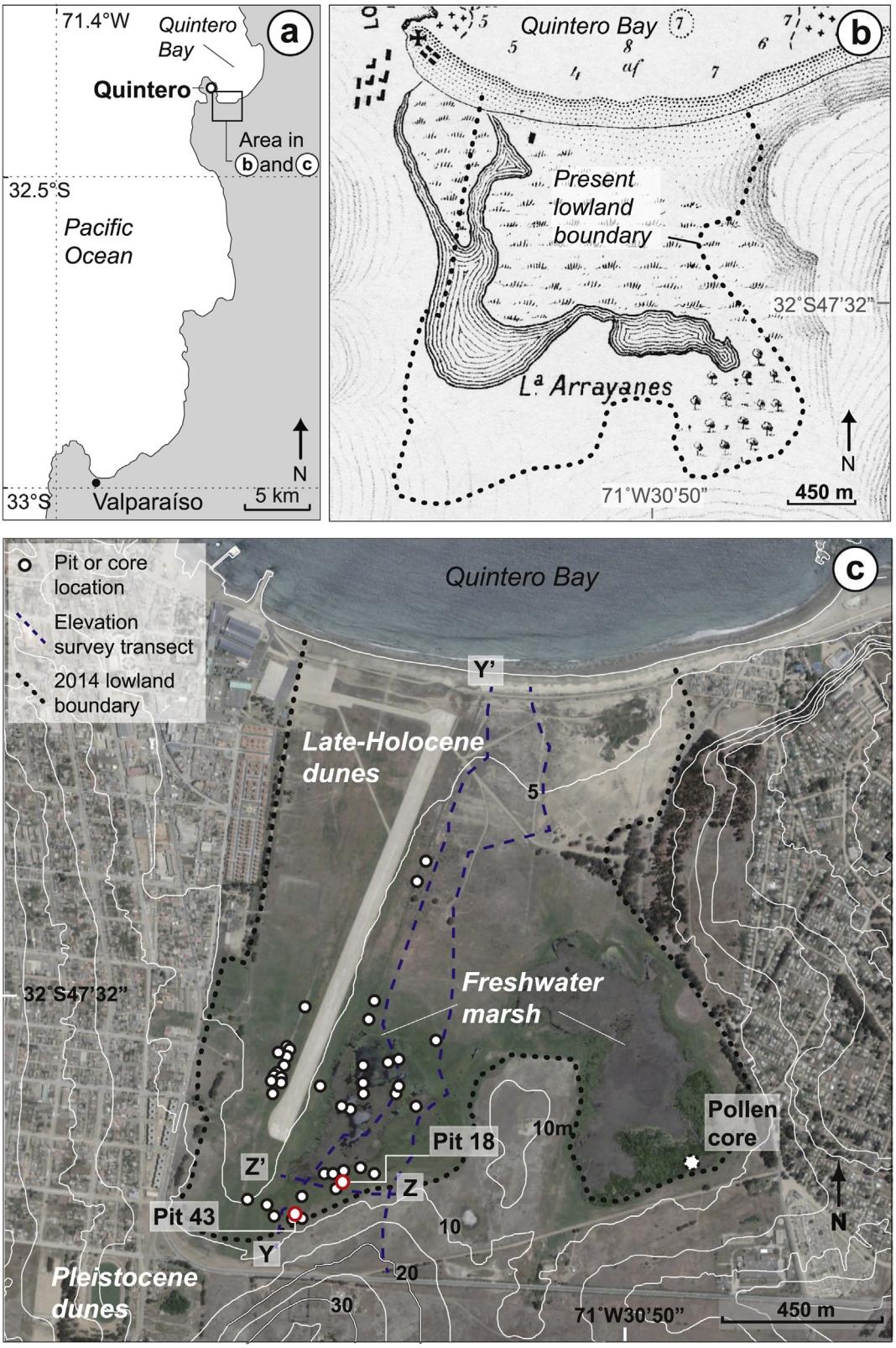

Fig. 3. a) Quintero Bay is located about 35 km north of the port city of Valparaíso. The city of Quintero and the Quintero lowland are located along the southern margin of the bay. b) Map of the Quintero lowland from AD 1876 showing a shallow lagoon, marsh, and forested areas covering the Quintero lowland. The boundary of the lowland (as shown in c) is marked by a black dotted line. c) Satellite Google Earth Pro, 2014 DigitalGlobe imagery of the Quintero lowland with a 10-m-contour topographic overlay. Described cores were projected onto three elevation transects, shown by blue dashed lines. The lowland is bordered by Pleistocene dunes to the south and a prograding dune sequence separates the marsh from the coast. The boundaries of the lowland are shown by a black dotted line. The location of the pollen core is approximate (Villa-Martínez and Villagrán, 1997). (For interpretation of the references to color in this figure legend, the reader is referred to the web version of this article.)

changes in relative sea level (RSL) (Plafker and Savage, 1970; Atwater, 1987). Sudden coseismic RSL rises or falls may create a series of distinctive, sharp lithologic contacts that record earthquakes over thousands of years (Plafker et al., 1992; Nelson et al., 1996; Witter et al., 2003). Widespread sand beds, deposited by tsunamis accompanying great earthquakes, are often found concomitant with lithologic evidence of sudden RSL change (Fig. 2; Sawai, 2001; Kelsey et al., 2002; Cisternas et al., 2005; Satake and Atwater, 2007).

Because of their sensitivity to environmental factors including salinity, tidal exposure, and substrate, microfossils incorporated into coastal sediments provide an independent test of earthquake-related RSL change and tsunami deposition inferred from coastal sequences (Fig. 2; Sherrod, 2001). Diatoms—long recognized as valuable RSL indicators—have been used to reconstruct earthquake and tsunami histories at several subduction zones (Hemphill-Haley, 1995a; Shennan et al., 1999; Sawai, 2001; Shennan and Hamilton, 2006). The utility of diatoms as RSL indicators also stems from the high preservation potential of their siliceous valves in coastal sedimentary archives (Hamilton et al., 2005; Sawai et al., 2008). Other siliceous microfossils such as phytoliths (siliceous plant remains) and chrysophyte cysts (freshwater golden algae) can be employed to similar advantage (Rebolledo et al., 2005).

Sedimentary archives of prehistoric earthquakes and tsunamis are scarce in central Chile because the combination of a semiarid climate, coseismic uplift rather than subsidence, and net Holocene emergence has resulted in limited accommodation space in which to preserve evidence (May et al., 2013). More extensive evidence has been found at wetter sites in southern and south-central Chile, although records are limited to the last ~2000 years (Atwater et al., 1992; Bartsch-Winkler and Schmoll, 1993; Cisternas et al., 2005; Moernaut et al., 2009; Nelson et al., 2009; Garrett et al., 2013; Ely et al., 2014; Moernaut et al., 2014).

Here, we present the first stratigraphic evidence of prehistoric earthquakes and tsunamis on the coast of metropolitan central Chile (Fig. 3). We used sedimentary and microfossil evidence from an unusual coastal lowland at Quintero to identify six tsunami deposits between 6200 and 3600 yrs BP. We observed evidence of coseismic uplift concurrent with five of the tsunamis. The limited time window of preservation of evidence for prehistoric seismicity discovered at Quintero reflects its RSL history, whose highest RSL peaked in the mid Holocene. We show how the geomorphic setting at Quintero created an environment favorable to the preservation of earthquake-related RSL change and tsunami inundation about the time of the RSL highstand. The ~2600 year window provides a glimpse into the recurrence of earthquakes with high tsunamis along a coast where historical records are too short to capture the repeated occurrence of its greatest events.

2. Tectonic and coastal setting

2.1. Earthquake deformation cycle in central Chile

The Chilean subduction zone marks the plate boundary between the subducting Nazca plate and the South American plate, extending 3500 km from the northern coast of Chile to the Chile triple junction offshore of southern Chile (Fig. 1a). Along the central Chilean subduction zone, the Nazca plate dips <10° and subducts to the northeast at 68–80 mm/yr (Pardo et al., 2002; Métois et al., 2012). Geodetic studies show that the central Chilean subduction zone is highly coupled. Plate-boundary asperities at ~30°S (the Challenger fracture zone offshore of Tongoy) and ~33°S (the Juan Fernandez Ridge offshore of Valparaíso) border the central Chilean segment and may limit rupture length (Métois et al., 2012).

Based on their accompanying tsunamis, the four largest historical plate-boundary earthquakes in central Chile occurred in AD 1730 (M ~9.0), 1822 (M 8.0–8.5), 1906 (M_w 8.4), and 1985 (M_w 7.8) (Comte et al., 1986; Barrientos, 1995; Ruegg et al., 2009). We exclude the AD 1575, 1580, and 1647 earthquakes from this sequence because there are no accounts of accompanying tsunamis; thus, there is a possibility that they were not megathrust earthquakes (Cisternas, 2012; Cisternas et al., 2012; Udías et al., 2012). The three most recent ruptures (AD 1822, 1906, and 1985) may have been limited in their southern extent by the Juan Fernandez Ridge asperity (Fig. 1b), but based on its widespread effects, the AD 1730 almost certainly extended south through the asperity.

The AD 1730 earthquake affected more than 800 km of the Chilean coastline, causing damage as far north as Copiapó and as far south as Concepción, which are 1000 km apart. The coastal city of Valparaíso was completely destroyed and Santiago sustained significant damage (Lomnitz, 1970; Udías et al., 2012). Damage from a high (>10 m) tsunami accompanying the AD 1730 earthquake stretched from La Serena in the north to Concepción in the south. The AD 1730 earthquake was at least as large as the 2010 Maule (M_w 8.8) earthquake but probably did not exceed the size of the 1960 Valdivia (M_w 9.5) earthquake, the two largest historical events in south central Chile (Udías et al., 2012). The sparse coastal population at the time of the AD 1730 earthquake resulted in probable undocumented widespread coastal deformation. However, considering that the last three plate-boundary earthquakes in the Valparaíso region produced coastal uplift (Lomnitz, 1970; Barrientos, 2007), we would expect the AD 1730 earthquake produced similar deformation.

The AD 1822, 1906, and 1985 earthquakes produced significant but more localized damage along the coast. The tsunamis accompanying the AD 1822, 1906, and 1985 events were lower (<4 m) than expected for the magnitude of the earthquakes (Moreno and Gibbons, 2007). The three earthquakes produced 0.4–1.2 m of coseismic uplift in and around Quintero (Comte et al., 1986). Thus, along the central Chilean subduction zone, historical earthquakes suggest that the earthquake deformation cycle is characterized by repeated instances of variable coseismic uplift interspersed with gradual interseismic subsidence, and deformation patterns for prehistoric earthquakes were probably at least as variable (Barrientos, 1996, 1997).

2.2. Quintero lowland

The Quintero lowland is located about 35 km north of Valparaíso and 70 km north of San Antonio, two of the largest ports in Chile (Figs. 1b and 3). The lowland (32.5°S) consists of a 1.2 km^2 coastal plain between 2 and 4 m above modern mean tide level (MTL). The lowland has no fluvial input and is isolated from the sea. Poor drainage and a high water table have allowed freshwater marsh vegetation to grow in a small area (0.3 km^2) in the southern lowland otherwise dominated by woodland, shrubland, and scrub vegetation (Fig. 3c; Villa-Martínez and Villagrán, 1997; Maldonado and Villagrán, 2006). Marsh plants *Scirpus americanus*, *Scirpus cernuus*, and *Scirpus inundatus* dominate the lower areas of the lowland, while *Sarcocornia fruticulosa*, *Atriplex prostrata*, and *Chenopodium frigidum* are found on higher ground (Villa-Martínez and Villagrán, 1997). Pleistocene dunes with elevations up to 80 m above MTL border the marsh. Pleistocene dunes are composed of mica-poor, poorly sorted fine and medium sand. A prograding late Holocene dune sequence (~4 m MTL) extends ~1 km inland, separating the marsh from the current coastline (Caviedes, 1972, Fig. 3c). In contrast to the Pleistocene dunes, the late Holocene dunes and beach sediment consist of mica-rich, well-sorted fine quartz sand

with little variation in particle size between summer and winter (Martínez et al., 2011).

The modern climate in the Quintero coastal region is semiarid with dry summers and wet winters (280 mm of rainfall per year), although winter droughts are not uncommon (Villa-Martínez and Villagrán, 1997). The modern Quintero coast is wave dominated and microtidal (Great Diurnal tidal range of ~1.6 m between MLLW–MHHW) as measured by the Chilean Hydrographic and Oceanographic service (SHOA) at Quintero. Two kilometers south of Quintero, the greatest incidence of wave direction is generally coincident with the predominant wind direction (from the W, SW, and NW) with maximum wave heights of 1–3 m (Martínez et al., 2011). No historical tropical cyclones have affected the Chilean coast because atmospheric circulation patterns preclude the formation of such low-pressure storm systems in the eastern South Pacific Ocean (Fedorov et al., 2010).

Palynology and historical records show the Quintero lowland has undergone significant environmental changes during the Holocene. Changes in pollen assemblages suggest that during the mid Holocene, the landward fringes of the Quintero lowland were part of an estuary and tidal marsh (Fig. 3c; e.g., Villa-Martínez and Villagrán, 1997; Maldonado and Villagrán, 2006). Assemblages within a sandy silt overlying basal Pleistocene sand indicate that sea level was higher prior to 5000 cal yr BP and that the lowland consisted of tidal flats and beach berms with patchy dune (grasses and small flowering plants) and sparse aquatic vegetation within interdunal depressions. At 4200 cal yr BP, a sharp increase in aquatic vegetation and brackish mollusks in fine silty sediment are consistent with tidal marsh and brackish lagoon environments. After 4000 cal yr BP, pollen assemblages show a decrease in aquatic vegetation and an increase in freshwater marsh vegetation suggesting decreased tidal inundation of the lowland during late-Holocene sea-level fall (Villa-Martínez and Villagrán, 1997). Since 2000 cal yr BP the vegetation and climate at Quintero were similar to the present (Maldonado and Villagrán, 2006). Historical maps from the AD 1700s and 1800s show a lowland environment similar to that of today, but include a lagoon covering parts of the lowland (Fig. 3b). The lagoon has since drained, probably due to human modifications. In general, the upper meter of sediment has undergone significant anthropogenic modification during 19th and 20th century construction projects aimed at preparing the lowland for residential development (never completed), and later a Chilean Air Force airstrip.

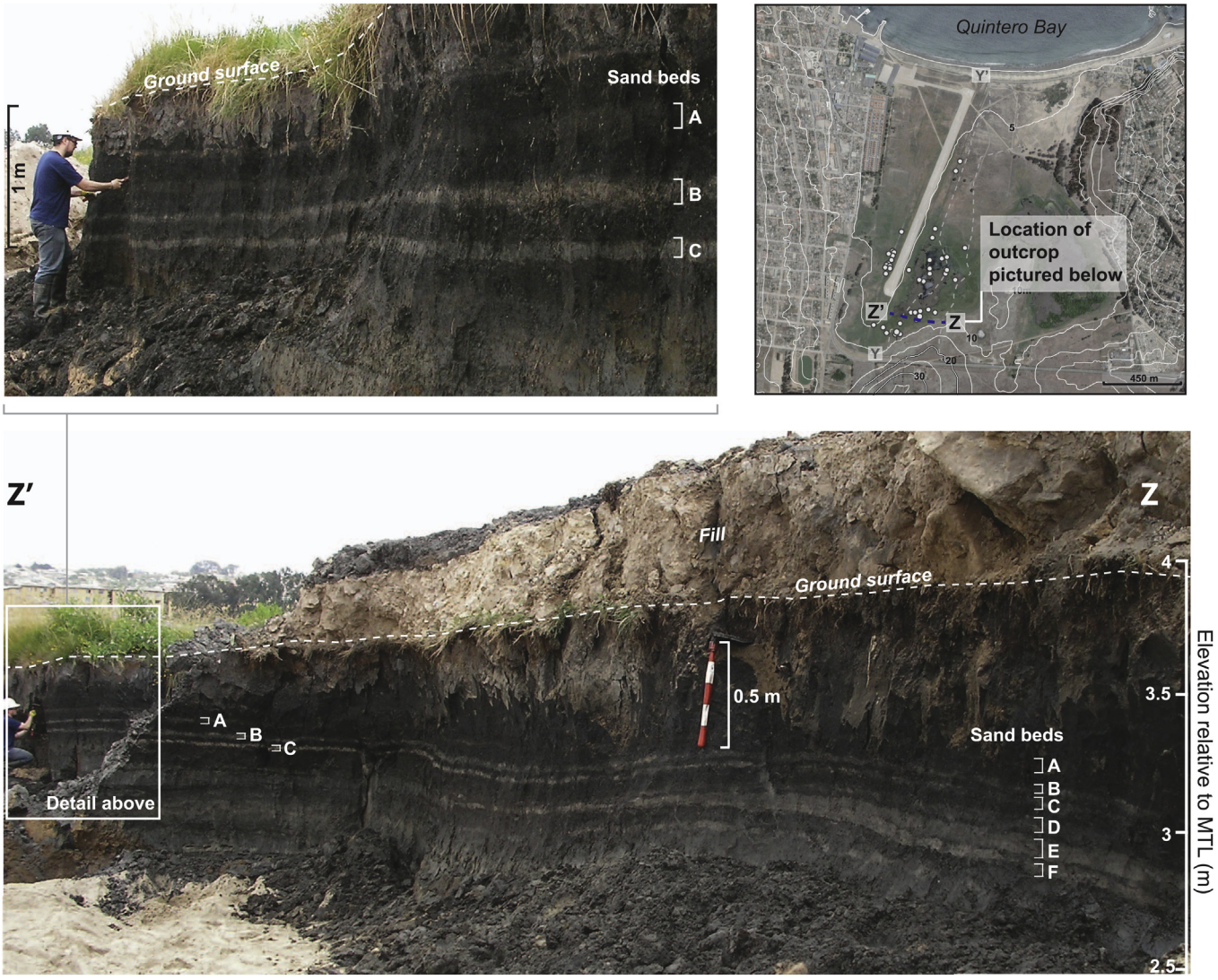

Fig. 4. Photographs and map showing an outcrop along the Z–Z′ elevation transect. Sand beds F-A are labeled.

3. Approach and methods

To decipher a history of coseismic land-level change during large earthquakes and tsunami deposition for the Quintero lowland, we described 57 cores, hand-dug pits, and exposures to a depth of 2–3 m (Fig. 3c). The Chilean Air Force, which currently occupies the lowland, dug 10- to 50-m long, ~2-m deep backhoe trenches for us during the construction of a new runway (Fig. 4). For coring, we used a 1-m-long, 25-mm-diameter, half-cylinder gouge corer. All sections were photographed and their lithology, color (Munsell soil color charts, 1975), and stratigraphy described in the field. We used a differential GPS system (Leica 1200) to survey the lowland (Fig. 5a). All elevations were tied into a benchmark and tidal datum maintained by the SHOA at Quintero, and reported as elevation (in meters) relative to MTL. Multiple transects perpendicular and parallel to the coast were completed and outcrop, core and pit locations were projected onto these transects with less than 15 cm vertical errors.

The most complete stratigraphic sequences were found along the slightly higher fringes of the coastal lowland (Fig. 5). We selected two pits from this area (Fig. 6; 43 and 18) for detailed analysis; monoliths were collected in the field and subsampled in the laboratory for grain-size distribution, organic content (loss on ignition), diatom analyses and radiocarbon dating.

3.1. Grain-size and loss on ignition analyses

For comparison of grain-size distributions among fossil and modern sediment, we collected modern surface (0–1 cm depth) samples from the beach bordering the lowland and the Pleistocene dunes (Fig. 7b). We sampled beach sediments in both summer and winter to account for seasonal variations in grain size. In fossil

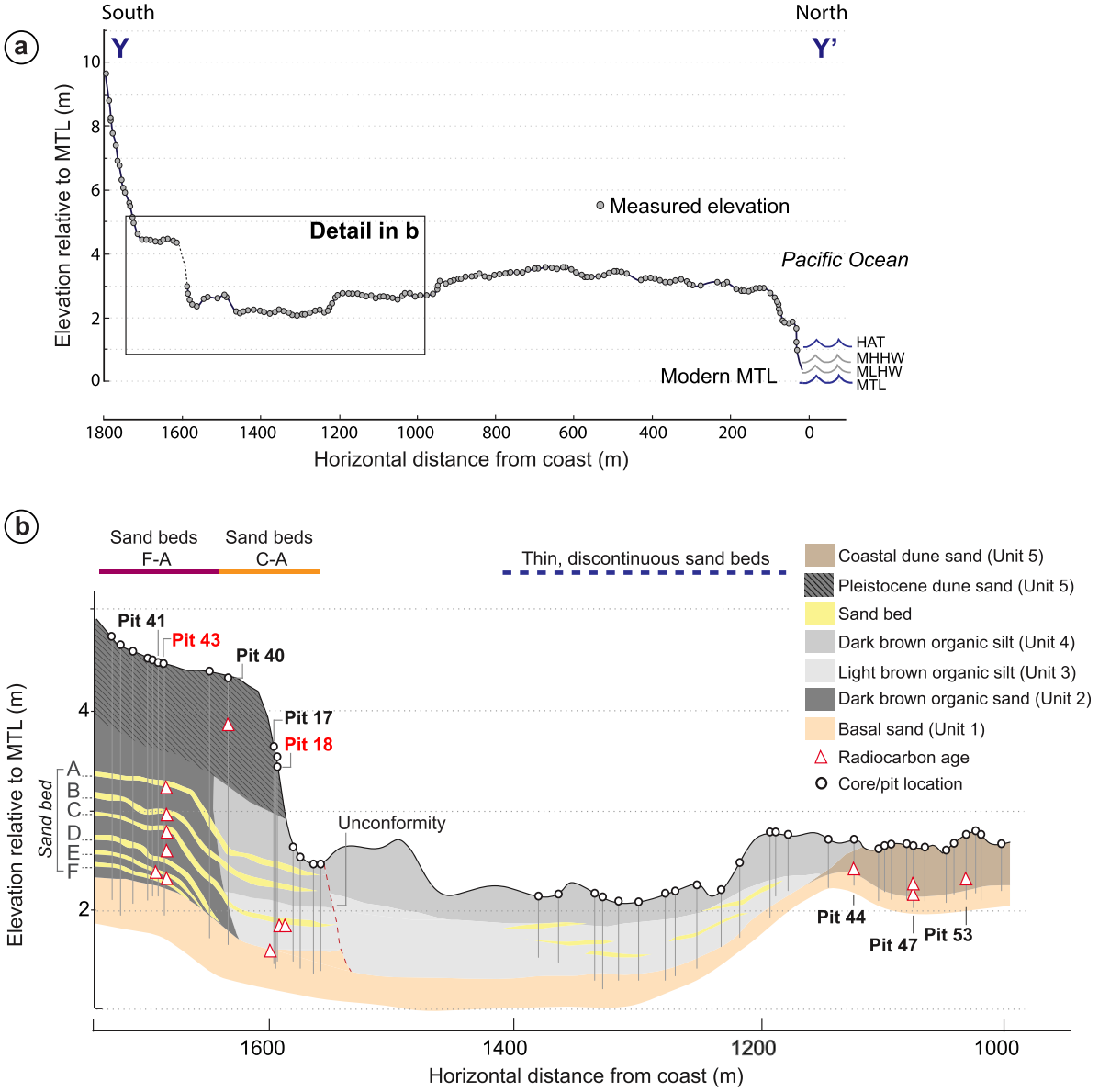

Fig. 5. a) Coast perpendicular elevation profile along transect Y–Y′ (see Fig. 3c for profile location). Elevations are relative to mean tidal level (MTL). Modern tidal datums mean lower high water (MLHW; 0.3 m), mean higher high water (MHHW; 0.6 m), and highest astronomical tide (HAT; 1.1 m) are shown on right. b) Detail of the Quintero lowland stratigraphy showing pit locations and radiocarbon sampling locations. Sands F-A are labeled. The extents of sand beds are plotted above the elevation profile. Pits chosen for detailed analysis (43 and 18) are highlighted in red. (For interpretation of the references to color in this figure legend, the reader is referred to the web version of this article.)

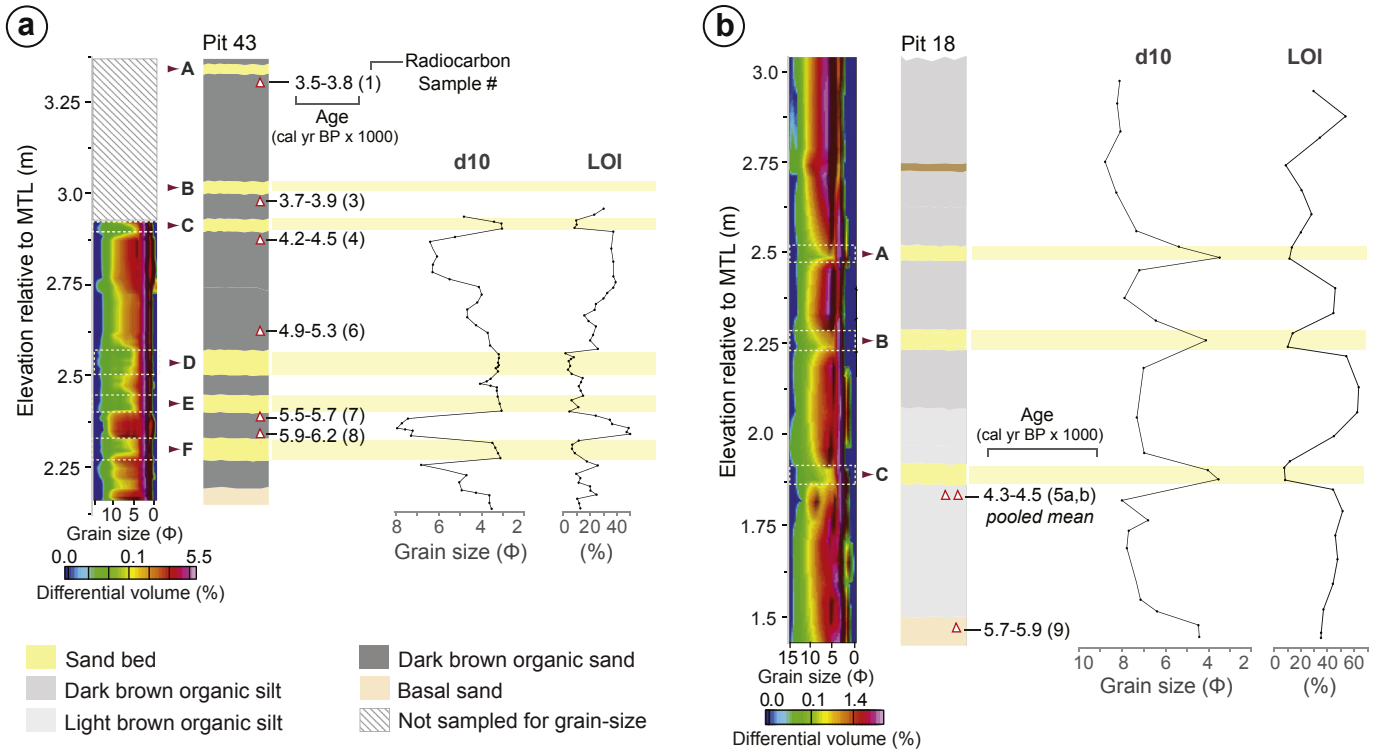

Fig. 6. a, b) High resolution grain-size distribution color surface plots (Φ) showing the differential volume of sediments (the percentage of total volume that each size class occupies), detailed lithology, D10 values (diameter at which 10% of a sample's mass comprises smaller grains), and LOI (weight %) for stratigraphic columns of pits 43 and 18. Elevations are relative to mean tide level (MTL). Radiocarbon sampling locations and calibrated radiocarbon ages are plotted on columns. Radiocarbon sample numbers correspond to sample numbers in Table 1.

sections, subsampling for grain size and loss on ignition (LOI) was conducted at 1 cm intervals near lithologic contacts and at 5 cm intervals in homogenous sediments.

Modern and fossil grain-size samples were treated with hydrogen peroxide (30%) to remove organic material and analyzed using a Beckman Coulter LS230 laser diffraction grain-size analyzer. Grain-size interpretations are based on the Wentworth Phi Scale and reported as differential volume (the percentage of total volume that each size class occupies). The grain-size distributions were interpolated and gridded using a triangular irregular network (TIN) algorithm (Sambridge et al., 1995) and plotted as color surface plots using Geosoft Oasis TM software (Donato et al., 2009). The mean grain size and D10 value (diameter at which 10% of a sample's volume comprises smaller particles) of each sample were used to characterize lithologic units.

Fossil samples for LOI (a proxy for the percentage of organic matter) were dried at 105 °C for 12 h, weighed, baked at 550 °C for 6 h, and weighed again to estimate the weight lost (Ball, 1964).

3.2. Diatom analysis

We subsampled the lower stratigraphy of pit 43 (including sand beds F-D) and upper stratigraphy of pit 18 (including sand beds C-A) for diatom analysis (Figs. 8 and 9). Subsampling intervals ranged from 2 cm near lithologic contacts to 15-cm intervals in homogenous sediment. To remove organic material, we oxidized ~1 g of sediment with nitric acid in a microwave digestion system (Charles, 2002). A known volume of digested sample (between 25 and 100 μl depending on the diatom concentration) was then pipetted and distributed evenly on a cover slip. The cover slip was dried overnight and then inverted and mounted on a glass slide using Naphrax (Charles, 2002). A total of 49 diatom slides were prepared from pits 43 and 18. Diatoms were identified to species level using a light microscope under oil immersion at 1000× magnification with reference to Krammer and Lange-Bertalot (1986, 1988, 1991a,b) and Lange-Bertalot (2000). When possible, 300 diatoms were identified and counted in slides with each species expressed as a percentage of total diatom valves counted. Fragments containing more than half a valve were included in the count. Only species that exceeded 5% of total valves counted were used for paleoecological interpretation (Horton and Edwards, 2006). We identified 49 species in 19 genera from 49 samples in pits 43 and 18. Diatoms were classified by salinity (marine, brackish, and freshwater) and life-form (planktonic, epipelic, epiphytic, aerophilic) based on the ecological preferences outlined in Chilean (Rivera, 2000; Rebolledo et al., 2005, 2011) and global (Krammer and Lange-Bertalot, 1986, 1988, 1991a,b; Hartley et al., 1986; Vos and de Wolf, 1988, 1993; Denys, 1991) catalogs.

The depositional environment (high-marsh/upland, brackish lagoon, low-marsh, or tidal flat) represented by each stratigraphic unit was determined based on a qualitative interpretation of the relative abundances of diatoms within salinity and life-form groups. The marine diatom group includes marine and marine-brackish species that thrive in salinities exceeding 30 practical salinity units (psu). The brackish diatom group includes brackish-marine and brackish species that tolerate salt concentrations between 0.2 and 30 psu. The freshwater group includes fresh-brackish and fresh diatoms that generally occur in salt concentrations less than 0.2 psu. Diatom taxa that live attached to plants are defined as epiphytic forms; taxa that live on wet sediments are defined as epipelic forms; taxa that live on wet sediments but are able to survive temporarily dry conditions are defined as aerophilic forms. Tychoplanktonic diatoms include an array of species that live in the benthos, but are commonly found in the plankton.

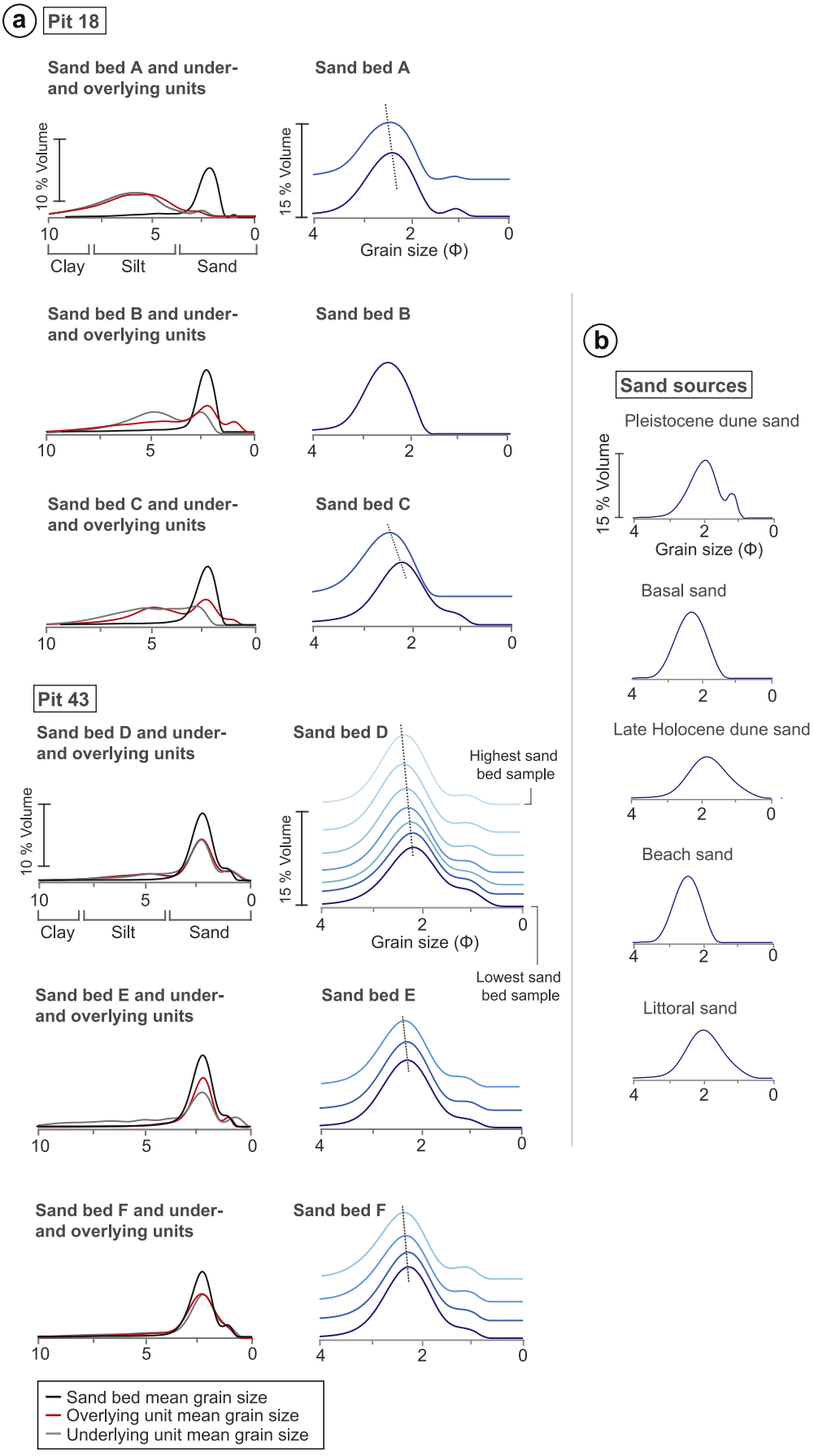

Fig. 7. a) Grain-size differential volume curves for stratigraphic units and sand beds F-A. Lines connecting differential volume curves show normal grading in sand beds. b) Grain size differential volume curves for modern surface sediments of the Quintero lowland.

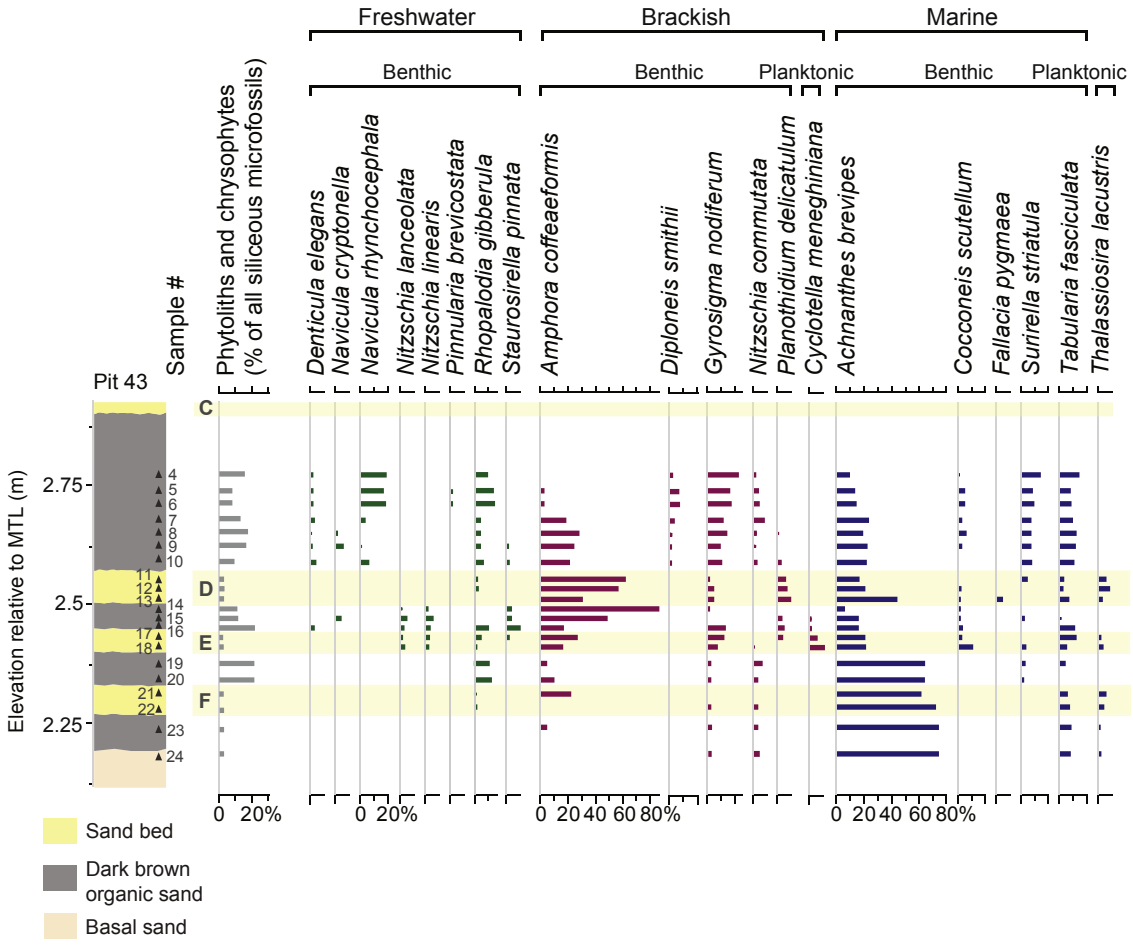

Fig. 8. Summary of microfossil analyses for pit 43. Triangle symbols on stratigraphic column show locations of numbered samples. Relative abundance of diatoms (showing only those species that are ecologically diagnostic) is expressed as a percent of the total count. Abundance of grass phytoliths and chrysophyte cysts expressed as a percent of total siliceous microfossils.

Diatoms that float in the water column and do not live attached to any substrate are defined as planktonic forms (Vos and de Wolf, 1988, 1993).

Samples were also scanned for the abundance of phytoliths and chrysophyte cysts to help distinguish freshwater from tidal environments. Phytoliths typical of brackish and fresh coastal grasses were identified to the subfamily level (Pooideae and Bambusoideae subfamilies) with reference to the classifications of Lu and Liu (2003).

To examine the pattern of diatom assemblage variation within and between samples, we used detrended correspondence analysis (DCA; Fig. 10). Samples with similar species compositions are grouped together in the DCA bi-plot and samples with statistically different species compositions plot apart (Horton and Edwards, 2006). The percent abundance of grass phytoliths and chrysophyte cysts were included in the DCA analysis.

3.3. Radiocarbon dating

Where possible, we collected plant macrofossils for radiocarbon dating from organic sediments that gave either limiting maximum ages (usually below each contact) or limiting minimum age (in growth position above each contact) to constrain the age of the sand beds in Pits 43 and 18 (Table 1). Following Kemp et al. (2013), we collected samples that were in growth position (rhizomes) or so delicate (e.g., seeds, leaf parts) that they would probably have decayed or been broken by transport soon after death, thus reducing the likelihood of dating material much older than contact burial. Radiocarbon ages were calibrated using OxCal radiocarbon calibration software (Bronk Ramsey, 2009) with the SHCal13 data set of Hogg et al. (2013). Calibrated age ranges are shown at two standard deviations where years 'before present' (BP) is years before AD 1950. We use maximum and minimum limiting radiocarbon ages to calculate age probability distributions for inferred tsunami beds from pits 43 and 18 with the V-sequence feature of OxCal (Fig. 11; Bronk Ramsey, 2008; e.g., DuRoss et al., 2011; Berryman et al., 2012). To estimate inter-event times and recurrence intervals of paleoearthquakes and tsunamis we used the "difference" function in OxCal.

4. Results

We observed five main lithostratigraphic units (units 1, 2, 3, 4, and 5) and six distinct sand beds (beds A, B, C, D, E, and F) that occur within units 2, 3, and 4 (Fig. 5b). A compact gray (5YR 7/1) basal sand containing very little organic material uniformly underlies the lowland between 1 and 2.5 m MTL (unit 1). Landward of 1650 m from the present coastline, a dark brown (10YR 2/1) organic sand (unit 2) overlies the basal sand (cf. pit 43). The organic sand is ~1.5 m thick and contains visible (5–10 mm long) herbaceous plant

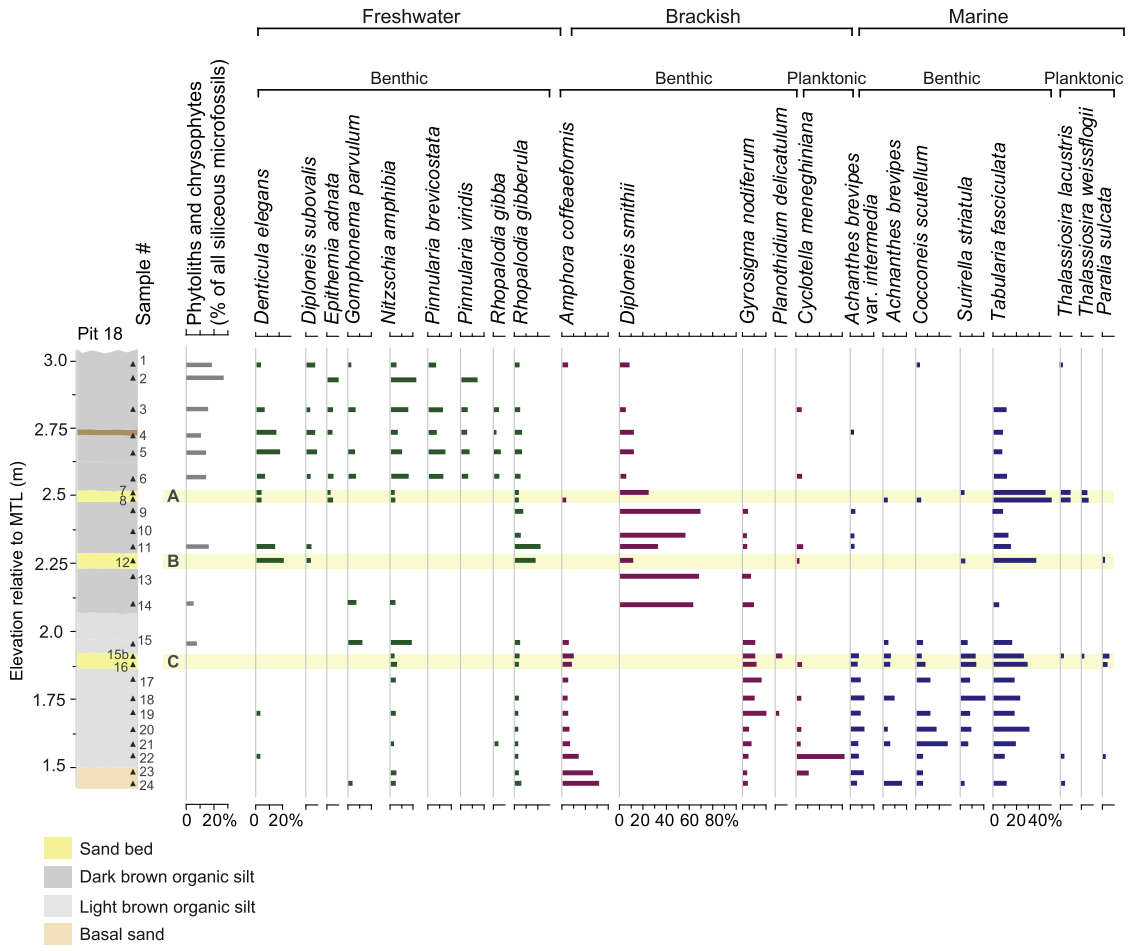

Fig. 9. Summary of microfossil analyses for pit 18. Triangle symbols on stratigraphic column show locations of numbered samples. Relative abundance of diatoms (showing only those species that are ecologically diagnostic) is expressed as a percent of the total count. Abundance of grass phytoliths and chrysophyte cysts expressed as a percent of total siliceous microfossils.

fragments. In landward locations between 1100 m and 1650 m, a light brown (10YR 5/3) organic silt (unit 3) overlies the basal sand. The unit is ~0.5 m thick and contains humified organic matter, but few identifiable herbaceous plant fragments. A dark brown (10YR 2/1) organic silt (unit 4) that is ~1 m thick overlies unit 3. It is distinguished from unit 3 by its darker color and the presence of visible (5–10 mm long) herbaceous plant fragments. Above the organic sands and silts is ~1 m of brown (10YR 4/3) reworked dune sand containing little organic material (unit 5). In landward locations the source of the sand is probably the adjacent Pleistocene dunes, whereas in seaward locations up to 1100 m from the present coastline, the source of the sand is likely the modern <1000-yr-old coastal dunes.

Six ~4-cm-thick sand beds are interbedded within the organic silt and sand (units 2, 3, and 4) and extend up to 200 m across the lowland. We labeled the sand beds from oldest (F) to youngest (A). All six sand beds can be correlated throughout unit 2. Units 3 and 4 only contain the three youngest beds (beds C, B, and A). Three thinner, discontinuous sand beds were found in more seaward sections (Fig. 5b). However, because we were not able to correlate these beds between sections and we are unsure of their origin, they will not be discussed further. Beds F-A were distinct from their host sediments due to their sharp (<1–3 mm) upper and lower contacts, lack of organic matter, uniform thickness, lateral extent, and planktonic marine fossils. Erosive contacts and rip-up clasts were observed in beds F, E, and D.

4.1. Basal sand

The basal sediments of pits 43 (2.10–2.20 m MTL) and 18 (1.40–1.50 m MTL) are composed of gray (5YR 7/1), well sorted, mica-rich, very fine quartz sand (unit 1; mean = 2.45 Φ; D10 = 4.38 Φ; Fig. 6a) and contain little organic material (LOI < 10%). Marine and brackish epiphytes (e.g. *Achnanthes brevipes* and *Tabularia fasciculata*) dominate basal sand diatom assemblages in both pits (Figs. 8 and 9). Pit 18 contains additional marine and brackish species including the marine epiphyte *Cocconeis scutellum*, the marine planktonic *Thalassiosira lacustris*, the brackish epipelon *Amphora coffeaeformis*, and the brackish tychoplanktonic *Cyclotella Meneghiniana* (Table 2).

In Pit 18, a fragile twig with leaf scars collected from the upper contact of the basal sand yields a maximum limiting age of 5655–5896 cal yr BP for the onset of Holocene sediment deposition in this portion of the lowland (Fig. 6b).

4.2. Sand bed F and under- and overlying units (Pit 43)

Between 2.20 and 2.28 m MTL, a dark brown, poorly sorted organic sand (unit 2; mean = 2.36 Φ; D10 = 4.96 Φ) overlies the basal sand in Pit 43 (Figs. 6a and 7a). The unit contains more organic material (LOI 25%) than the underlying basal sand, but diatom assemblages are similar, with an assemblage dominated by the marine diatoms *A. brevipes* and *T. fasciculata* (Fig. 8).

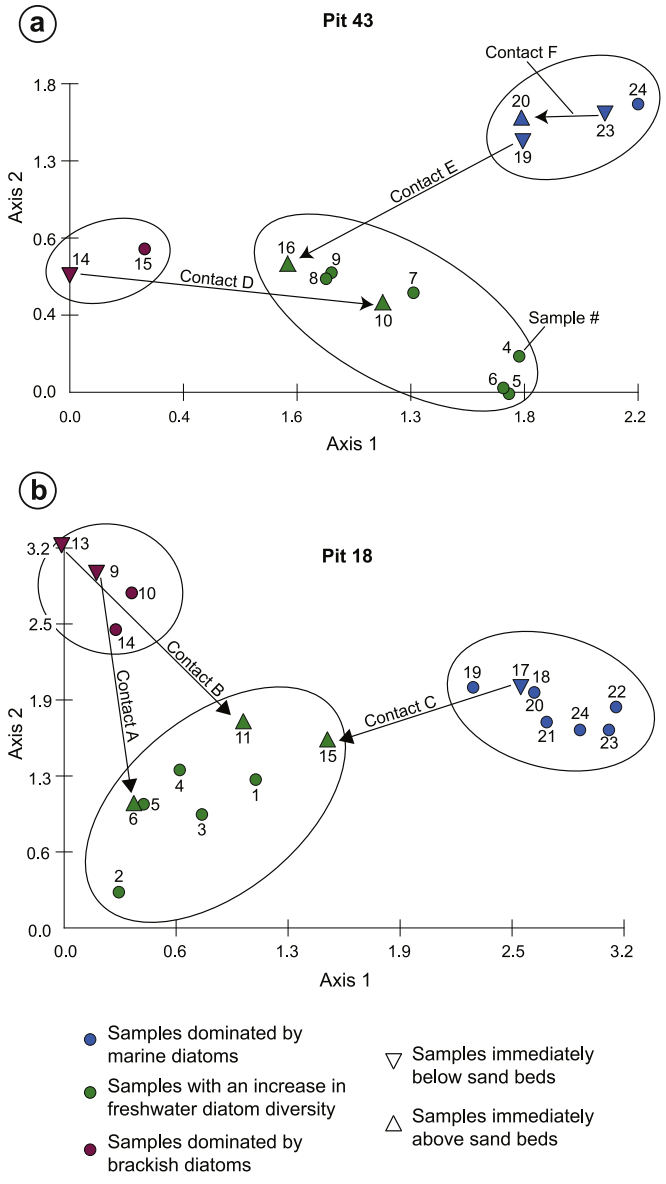

Fig. 10. Results of detrended correspondence analysis (DCA) for diatom samples from Pit 43 (a) and Pit 18 (b). Samples with similar species compositions are grouped together in the DCA bi-plot and samples with statistically different species compositions plot apart (Horton and Edwards, 2006). The percent abundance of grass phytoliths and chrysophyte cysts are included in the DCA analysis. Arrows show how assemblage bi-plot scores change from below to above labeled bed contacts.

At 2.28 m MTL, an erosive contact separates unit 2 from bed F, a 4-cm-thick, tan, well sorted, mica-rich, fine quartz sand (mean = 2.26 Φ; D10 = 3.22 Φ) containing little organic material (LOI < 10%). The sand bed contains rip-up clasts from the underlying unit. Although bed F contains a marine and brackish diatom assemblage similar to that of the underlying sediment, there is an increase in the marine planktonic *T. lacustris*. A decreased fine fraction—shown by a decrease in D10 value—distinguishes the grain size of bed F from under- and overlying sandy units. Four grain-size samples taken at 1 cm vertical intervals show subtle upward fining and an increased fine fraction towards the top of the bed (Fig. 7a).

A dark brown, poorly sorted organic (LOI 28%) sand (unit 2; mean = 2.54 Φ; D10 = 7.23 Φ) overlies bed F at 2.33 m MTL. Diatom assemblages within this organic sand are similar to assemblages underlying bed F. But there is an increase in the freshwater epiphyte *Rhopalodia gibberula* and grass phytoliths and chrysophyte cysts within the overlying unit (Fig. 8). The DCA reflects this increase in freshwater taxa with a subtle change in DCA sample scores between units below and above the bed (Fig. 10a).

A rhizome collected from the organic sand immediately overlying bed F yields a minimum limiting age for sand deposition of 5931–6182 cal yr BP (Fig. 6a).

4.3. Sand bed E and under- and overlying units (Pit 43)

At 2.38 m MTL, an erosive contact separates unit 2 from bed E, a 3-cm-thick, tan, well sorted, mica-rich, fine quartz sand (mean = 2.23 Φ; D10 = 3.10 Φ; Figs. 6a and 7a) containing little organic material (LOI 8%). The sand bed contains rip-up clasts from the underlying unit. Diatom assemblages within bed E are dominated by marine and brackish species, including planktonic species (e.g., *T. lacustris* and *C. meneghiniana*) not found in units under- and overlying the bed. Dominant marine and brackish diatoms in the lower 1 cm of bed E include *A. brevipes*, *A. coffeaeformis*, and *C. scutellum*. In the upper centimeter of bed E, *A. coffeaeformis*, *T. fasciculata*, and the brackish epipelon *Gyrosigma nodiferum* increase in abundance (Fig. 8). A decreased fine fraction distinguishes the grain size of bed E from under- and overlying sandy units. Three grain-size samples taken at 1 cm vertical intervals show subtle upward fining and an increased fine fraction towards the top of the sand bed (Fig. 7a).

A dark brown, poorly sorted organic (LOI 32%) sand (unit 2; mean = 2.28 Φ; D10 = 3.46 Φ) overlies bed E at 2.44 m MTL. Within this organic sand, there is a notable increase in freshwater diatoms (e.g., *Navicula tripuncta*, *Nitzschia lanceolata*, *Nitzschia linearis*, *R. gibberula* and *Staurosirella pinnata*) compared to the marine dominated diatom assemblage in sediments underlying bed E. The significant increase in freshwater diatom diversity and abundance above the sand bed is reflected by a shift in DCA sample scores from marine to freshwater dominated samples (Fig. 10a).

A rhizome collected from the organic sand immediately underlying bed E yields a maximum limiting age for sand deposition of 5492–5732 cal yr BP (Fig. 6a).

4.4. Sand bed D and under- and overlying units (Pit 43)

The diatom assemblage in the dark brown, poorly sorted organic sand (LOI 29%) immediately underlying bed D at 2.4 m MTL is dominated by the brackish diatom *A. coffeaeformis* (85%). At 2.5 m MTL, an erosive contact separates unit 2 from bed D, a 7-cm-thick, tan, well sorted, mica-rich, fine quartz sand (mean = 2.20 Φ; D10 = 3.15 Φ; Figs. 6a and 7a) containing little organic material (LOI < 5%). The sand bed contains rip-up clasts from the underlying unit. The diatom assemblage within bed D is dominated by marine and brackish species (e.g., *A. brevipes*, *A. coffeaeformis*, *T. fasciculata*, and *Planothidium delicatulum*), including the marine planktonic *T. lacustris*, not found in the organic units under and overlying the bed (Fig. 8). *A. brevipes* is abundant in the lower 3 cm of bed D and decreases in the top 4 cm of the deposit while *A. coffeaeformis* increases. A decreased fine fraction distinguishes the grain size of bed D from under- and overlying organic sandy units. Seven grain-size samples taken at 1 cm vertical intervals show subtle upward fining in the bed (Fig. 7a).

A dark brown, poorly sorted organic (LOI 35%) sand (unit 2; mean = 2.36 Φ; D10 = 4.85 Φ) overlies bed D at 2.56 m MTL. Within this organic sand, there is an increase in freshwater (e.g., *R. gibberula*, *Navicula rhynchocephala*, and *Denticula elegans*), brackish (*G. nodiferum*), and marine (e.g. *A. brevipes*, *T. fasciculata*)

Table 1
Radiocarbon age determinations, Quintero, Chile.

Sample #[a]	Pit[b]	Elevation MTL (m)	Sand	Radiocarbon Laboratory number	Lab reported age (^{14}C yr BP)	Calibrated age (cal yr BP − 2σ)	Maximum or minimum limiting age[c]	Description of dated material
1	43	3.3	A	302252	3660 ± 40	3830–4085	Maximum	Charcoal fragment immediately below Sand bed A
2	43	3.3	A	302253	3450 ± 30	3567–3821	Maximum	Rhizome sheath immediately below Sand bed A
3	43	2.98	B	302251	3600 ± 40	3711–3974	Maximum	Rhizome sheath immediately below Sand bed B
4	43	2.87	C	302250	3980 ± 40	4242–4519	Maximum	Rhizome sheath immediately below Sand bed C
5a	18	1.88	C	295081	4020 ± 30	4297–4529	Maximum	Rhizome fragment immediately below Sand bed C
5b	18	1.88	C	293371	3950 ± 40	4160–4509	Maximum	Twig immediately below Sand bed C
5a,b pooled mean	18	n/a	C	n/a	n/a	4291–4517	Maximum	n/a
6	43	2.62	D	302254	4440 ± 30	4857–5259	Minimum	Rhizome sheath 0.07 m above Sand bed D
7	41	2.37	E	302248	4940 ± 40	5492–5732	Maximum	Twigs immediately below Sand bed E
8	43	2.33	F	302249	5310 ± 40	5931–6182	Minimum	Charcoal fragments immediately above Sand bed F
9	17	1.47	Basal sand	293373	5060 ± 40	5655–5896	Maximum	Twigs in the top 0.03 m of the basal sand
10	40	3.85	n/a	306347	260 ± 30	148–321	Maximum	Twig or stem below thin, discontinuous sand
11	47	2.35	n/a	306351	1740 ± 30	1539–1701	Maximum	Charcoal within white precipitate layer
12	47	2.3	n/a	306352	2010 ± 30	1839–2001	Minimum	Charcoal above thin, discontinuous sand
13	44	2.45	n/a	306348	3620 ± 30	3726–3980	Minimum	Small gastropod above a mixed marl and sand unit
14	53	0.55	n/a	306354	200 ± 30	0–292	Minimum	Small gastropod above discontinuous sand layer

Maximum ages are on samples containing carbon judged to be older than a sand bed. Minimum ages are on samples judged younger than a sand bed.
[a] Sample ID's and corresponding sampling locations can be found on Fig. 6a,b.
[b] Pits with corresponding radiocarbon age locations can be found on Fig. 5b.
[c] Interpretation of the stratigraphic context of the dated sample relative to the time that host unit was deposited.

diatoms and a significant decrease in the brackish *A. coffeaeformis* compared to the brackish dominated assemblage in sediments underlying bed D. DCA sample scores above bed D reflect the significant change in species composition (Fig. 10a). Similar diatom assemblages are found in the organic unit up to 2.79 m MTL, with small increases in freshwater species observed at 2.7 m MTL.

A rhizome collected from the organic sand above bed D yields a minimum limiting age for sand deposition of 4856–5260 cal yr BP (Fig. 6a).

4.5. Sand bed C and under- and overlying units (Pit 18)

Between 1.5 and 1.89 m MTL, a light brown, very poorly sorted organic (LOI 37%) silt (unit 3; mean = 3.41 Φ; D10 = 6.88 Φ; Figs. 6b and 7a) overlies the basal sand in Pit 18. Like the underlying basal sand, diatom assemblages in the organic silt are dominated by marine (e.g., *T. fasciculata*, *A. brevipes var. intermedia*, *A. brevipes*, and *C. scutellum*) and brackish (e.g., *G. nodiferum* and *Surirella striatula*) species (Fig. 9).

At 1.89 m MTL, a sharp contact separates unit 3 from bed C, a 4-cm-thick, gray, well sorted, mica-rich, fine quartz sand (mean = 2.45 Φ; D10 = 3.77 Φ; Figs. 6b and 7a) containing little organic material (LOI < 6%). The diatom assemblage within bed C is dominated by marine and brackish diatoms (e.g., *T. fasciculata*, *A. brevipes var. intermedia*, *A. brevipes*, *S. striatula* and *G. nodiferum*) including the planktonic *Paralia sulcata*, which is not found in organic units under- and overlying the sand bed (Fig. 9). An increase in mean grain size and a decreased fine fraction distinguishes bed C from under- and overlying silty sediments by (Fig. 7a).

A light brown, very poorly sorted organic (LOI 40%) silt (unit 3; mean = 3.20 Φ; D10 = 7.13 Φ) overlies bed C at 1.93 m MTL. Within this organic silt, there is an increase in freshwater and fresh-brackish diatoms (e.g., *Nitzschia amphibia*, *Gomphonema parvulum*, and *Nitzschia frustulum*) and grass phytoliths and chrysophyte cysts compared to the marine dominated assemblage in sediments underlying bed C. The significant increase in freshwater diatom diversity and abundance above the bed is reflected by a shift in DCA sample scores from marine to freshwater dominated samples (Fig. 10b).

A rhizome and a piece of charcoal collected from the organic silt immediately below bed C yield statistically indistinguishable maximum limiting ages of sand deposition (4297-4529 and

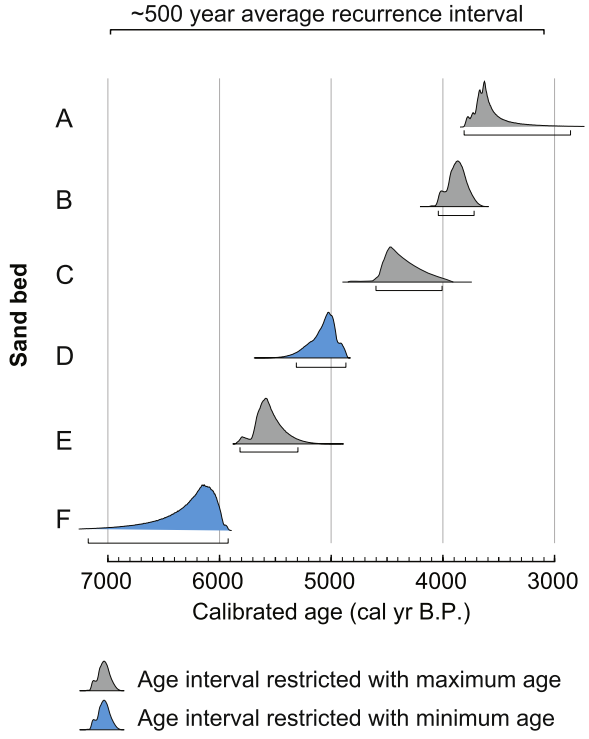

Fig. 11. Age probability distributions (brackets show 2σ interval) for inferred tsunami-deposited beds from pits 43 and 18 calculated using the V-sequence feature of OxCal. Distributions limited by a maximum age are purple; those limited by a minimum age are blue (Table 1). The average recurrence interval of inferred tsunamis is ~500 years. (For interpretation of the references to color in this figure legend, the reader is referred to the web version of this article.)

Table 2
Ecology of diagnostic diatom species.

Species (>5% abundance)	Ecology[a]	Ecology[b]	Ecology[c]	Life form[c]
Achnanthes brevipes	M & B	B & M	M & B	Epiphytic
Achnanthes brevipes var. intermedia	M & B	B & M	M & B	Epiphytic
Planothidium delicatulum	B	B	B & M	Epipsammic
Amphora coffeaeformis	M & B	B	–	Epipelic
Amphora ovalis	FW	FW	FW	Epipelic
Cocconeis scutellum	M & B	M & B	M & B	Epiphytic
Cocconeis diminuta	B	FW & B	B & FW	Epiphytic
Cyclotella meneghiniana	B	B	B	Tychoplanktonic
Cymbella pusilla	FW	FW & B	–	–
Cymbella silesiaca	FW	FW & B	–	Epipelic
Denticula elegans	FW	FW & B	–	Aerophilic & Epiphytic
Diploneis smithii	B	B & M	B & M	Epipelic
Diploneis subovalis	FW	FW & B	–	Epipelic
Epithemia adnata	FW	FW & B	FW	Epiphytic
Fallacia pygmaea	M & B	M & B	–	Epipelic
Staurosirella pinnata	FW	FW & B	FW & B	Planktonic & Epipelic
Gomphonema parvulum	FW	FW & B	FW	Aerophilic & Epiphytic
Gyrosigma nodiferum	B	B & FW	B	Epipelic
Navicula cryptotenella	FW	FW & B	–	Epipelic
Navicula libonensis	FW	FW & B	–	Epipelic
Navicula reinhardti	FW	FW & B	–	Epipelic
Navicula rhynchocephala	FW	FW & B	B	Epipelic
Navicula tripunctata	B	FW & B	–	Epipelic & Epiphytic
Nitzschia amphibia	FW	FW & B	FW	Aerophilic & Epiphytic
Nitzschia frustulum	FW	FW & B	–	Aerophilic & Epiphytic
Nitzschia lanceolata	B	B	–	Epipelic & Epiphytic
Nitzschia linearis	FW	FW	–	Epipelic
Paralia sulcata	M & B	M & B	M	Planktonic
Pinnularia brevicostata	FW	FW	–	–
Pinnularia viridis	FW	FW	FW	Aerophilic
Rhopalodia gibba	FW	FW	FW & B	Epiphytic
Rhopalodia gibberula	FW	–	–	Epiphytic
Surirella striatula	M & B	B & M	–	Epipelic
Tabularia fasciculata	M & B	B & M	M & B	Epiphytic
Thalassiosira lacustris	M & B	M & B	M	Planktonic
Thalassiosira weissflogii	M & B	B & M	M	Planktonic

[a] From Krammer and Lange-Bertalot (1986, 1988, 1991a,b). Marine = M; Brackish = B; Freshwater = FW.
[b] From Denys (1991).
[c] From Vos and de Wolf (1988, 1993). Planktonic = diatoms that float freely in the water column and do not live attached to any substrate; Tychoplanktonic = diatoms that live in the benthos, but are commonly found in the plankton; Epipelic = diatoms that live on or just below the surface of wet muddy sediments; Epiphytic = diatoms that are attached to larger plants or other surfaces; Aerophilic = diatoms that are able to survive subaerial, temporarily dry conditions.

4160–4509 cal yr BP). The pooled mean of the ages is 4291–4517 cal yr BP (Fig. 6b).

4.6. Sand bed B and under- and overlying units (Pit 18)

The light brown organic silt above bed C is replaced by a darker brown (LOI 50%), very poorly sorted organic silt at 2.08 m MTL (unit 4; mean = 3.60 Φ; D10 = 6.99 Φ; Figs. 6b and 7a). The diatom assemblage within the dark brown organic silt is dominated by the brackish diatom *Diploneis smithii*. At 2.24 m MTL, a sharp contact separates unit 4 from bed B, a 3-cm-thick, brown, well sorted, mica-rich, fine quartz sand (mean = 2.65 Φ; D10 = 4.08 Φ; Figs. 6b and 7a) containing little organic material (LOI < 5%). Bed B contains a mixed diatom assemblage including marine (e.g., *T. fasciculata*), brackish (e.g., *S. striatula*) and freshwater (e.g., *D. elegans*, *R. gibberula*, and *D. smithii*) species (Fig. 9). The marine and brackish planktonics *P. sulcata* and *T. lacustris*, not found in under- and overlying organic units, are observed in bed B. An increase in mean grain size and a decreased fine fraction distinguishes bed B from under- and overlying silty sediments (Fig. 7a).

A dark brown very poorly sorted, organic (LOI 51%) silt (unit 4; mean = 3.83 Φ; D10 = 7.17 Φ) overlies bed B at 2.27 m MTL. Within this organic silt, there is an increase in freshwater diatoms (e.g., *R. gibberula*, *D. elegans*, and *Diploneis subovalis*) and an increase in grass phytoliths and chrysophyte cysts compared to the brackish dominated assemblage in sediments underlying bed B. The significant increase in freshwater diatom diversity and abundance above the sand bed is reflected by a shift in DCA sample scores from brackish to freshwater dominated samples (Fig. 10b).

A rhizome collected from the organic silt immediately underlying bed B yields a maximum limiting age for sand bed deposition of 3711–3974 cal yr BP (Fig. 6b).

4.7. Sand bed A and under- and overlying units (Pit 18)

At 2.35 m MTL, the brackish diatom *D. smithii* (Fig. 9) increases in abundance and remains the dominant species within the dark brown organic silt until 2.45 m MTL, when the unit is sharply overlain by bed A, a 3-cm-thick, organic rich (LOI 48%), well sorted, mica-rich, fine quartz sand (mean = 2.56 Φ; D10 = 4.44 Φ; Figs. 6b and 7a). Diatom assemblages within bed A are dominated by marine species (e.g., *T. fasciculata*) including the marine planktonic diatoms *T. lacustris and Thalassiosira weissflogii*, not found in organic units under- and overlying the sand bed (Fig. 9). An increase in mean grain size and a decreased fine fraction distinguishes bed A from under- and overlying silty sediments. Bed A shows upward fining and an increased fine fraction towards the top of the bed (Fig. 7a).

A dark brown, very poorly sorted organic (LOI 45%) silt (unit 4; mean = 4.86 Φ; D10 = 8.31 Φ) overlies bed A at 2.48 m MTL. Within this organic silt, there is an increase in freshwater diatoms (e.g., *D. elegans*, *Pinnularia brevicostata*, and *N. amphibia*) and grass phytoliths and chrysophyte cysts compared to the brackish dominated assemblage in sediments underlying bed A. The significant increase in freshwater diatom diversity and abundance above the bed is reflected by a shift in DCA sample scores from brackish to freshwater dominated samples (Fig. 10b). Diatom assemblages for the remainder of Pit 18 are dominated by freshwater species.

A rhizome collected from the organic silt immediately underlying bed A yields a maximum limiting age for sand bed deposition of 3567–3821 cal yr BP (Fig. 6b).

5. Discussion

Based on stratigraphy, lithology (grain-size distribution and LOI), diatom, and radiocarbon analyses, we infer the depositional environment represented by each lithologic unit and the timing of environmental changes. In the ~6000 years represented by the lithofacies in our most complete stratigraphic sections, diatom assemblages indicate that the geomorphology of the Quintero lowland was significantly different than today. Diatoms show the landward fringes (where pits 43 and 18 are located) of the lowland transitioned from a mostly marine and brackish environment in the early Holocene to a freshwater marsh environment by the mid to late Holocene (Figs. 8 and 9). Within this long-term freshening trend, diatoms fluctuate back and forth between marine and/or brackish dominated assemblages and brackish and/or freshwater assemblages punctuated by widespread, anomalous sand beds, which we interpret below to have been deposited by tsunamis. We infer that the unusually sudden and long lasting changes in diatom assemblages associated with five of the six sand beds signal sudden RSL falls during times of decimeter-scale coseismic uplift.

5.1. Evidence for tsunami deposition

We infer a tsunami origin for the six sand beds within the Quintero lowland sequence. We base our interpretation on characteristics shared by all six beds including: significant lateral extent, uniform thickness, sharp (1–3 mm) lower and upper contacts, mixed diatom assemblages that include anomalous marine planktonic species, mica content, and upward fining sequences. Such characteristics have been found in modern tsunami deposits from Papua New Guinea (e.g., Gelfenbaum and Jaffe, 2003; Dawson, 2007), Thailand (e.g., Jankaew et al., 2008; Sawai et al., 2008), Sumatra (e.g., Monecke et al., 2008), Chile (e.g., Cisternas et al., 2005; Horton et al., 2011; Garrett et al., 2013; Ely et al., 2014), and Japan (e.g., Goto et al., 2011; Szczuciński et al., 2012). Beds F-A can be correlated over distances of 100–200 m. Radiocarbon ages from plant macrofossils underlying bed C in pits 18 and 43 are statistically indistinguishable, consistent with lateral continuity of this bed. Beds F, E, and D have erosive lower contacts and sharp upper contacts and contain rip-up clasts of material reworked during inferred high-energy, turbulent flows (e.g., Goff et al., 2012). Beds C, B, and A also display sharp upper and lower contacts but lack rip-up clasts. The lateral continuity and tabular geometry of the sand beds rule out localized processes, such as tidal channel migration, liquefaction, or sand venting during earthquakes as the process responsible for sand bed deposition (e.g., Atwater et al., 1992; Allen, 2000; Williams et al., 2005; Arcos, 2012).

We infer that the marine, brackish, and freshwater diatoms in all six sand beds reflect tsunami surges and subsequent backflows across subtidal, intertidal and supratidal environments of the lowland (e.g., Hawkes et al., 2007; Sawai et al., 2009; Horton et al., 2011; Szczuciński et al., 2012). The presence of anomalous marine and brackish planktonic species (e.g., *T. weissflogii*, *T. lacustris*, *C. meneghiniana*, and *P. sulcata*) in the sand beds supports a tidal-flat or subtidal source for the sediment and eliminates a fluvial source (Figs. 12b and 13b; e.g., Hemphill-Haley, 1996; Sawai et al., 2008). Our analysis of likely paleo-sediment sources shows that the sand in the inferred tsunami beds was mostly derived from beach and dune erosion. Possible sediment sources for the inferred tsunami beds include the Pleistocene dunes bordering the lowland, the basal tidal flat sand underlying the lowland, and the late Holocene dune, beach, and littoral sand. The Pleistocene dune sand is composed of brown, poorly sorted, fine and medium sand with no mica (mean = 1.87 Φ; D10 = 2.56 Φ; Fig. 7b), whereas the basal tidal flat sand and late Holocene dune, beach, and littoral sands are composed of tan or gray, well sorted, mica-rich, very fine and fine quartz sand (mean = 2.45 Φ; D10 = 4.38 Φ). All inferred tsunami beds display similar characteristics to the basal tidal flat sand and late Holocene coastal sediment; beds are composed of well sorted, mica-rich, fine quartz sand (Fig. 7b). The physical characteristics of the sand beds and the presence of mica, which is not found in the Pleistocene dunes, make aeolian deposition unlikely (e.g., Sawai et al., 2012).

All but one sand bed (bed B is the exception) drapes preexisting paleo-topography and displays upward fining and an increased fine fraction towards the top of the bed. These features are indicative of sediment settling out of suspension as a tsunami flow decelerates after reaching its inland extent (Fig. 7a; Gelfenbaum and Jaffe, 2003; Morton et al., 2007; Jaffe et al., 2011). Diatom analyses also reveal grading of diatom valves, a feature interpreted to reflect variable flow speed in the 2004 Indian Ocean tsunami and 2010 south-central Chile tsunami (Sawai et al., 2009; Horton et al., 2011). In sands F, E, and D, larger diatoms such as *A. brevipes* (>50 μm; thick, oval shaped valve) were abundant at the bottom of the sand beds while silt-sized diatoms such as *A. coffeaeformis* (<30 μm; narrow valve) increased in abundance towards the top of the beds.

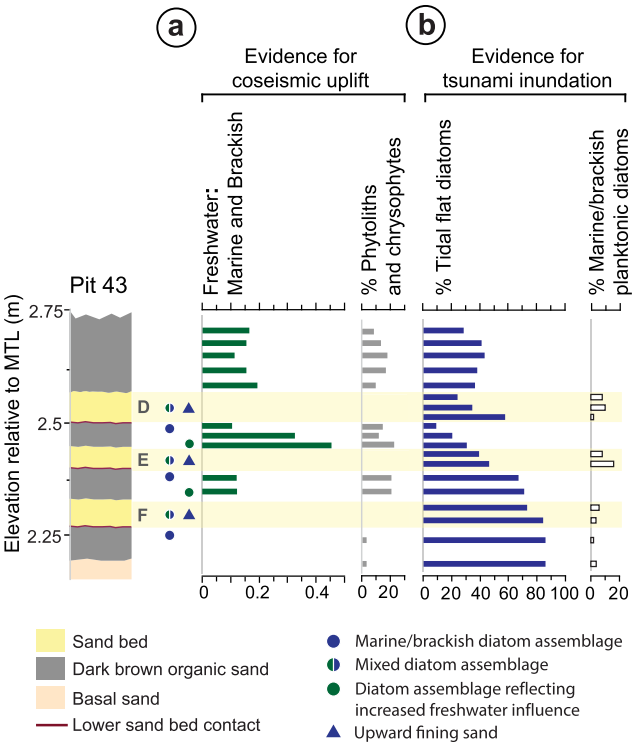

Fig. 12. Summary of evidence for coseismic uplift and tsunami inundation for pit 43. Symbols showing the nature of diatom assemblages and upward fining sequences correspond to the schematic drawing in Fig. 2. a) The summary of evidence for coseismic uplift highlights the increase in the ratio of freshwater to marine and brackish diatoms above sand beds as well as the increase in grass phytoliths and chrysophyte cysts above the sand beds. The microfossil content of the sands is left out to highlight the change in assemblages across the beds. b) Evidence for tsunami inundation includes the high relative abundance of tidal flat diatoms within sand beds and the presence of marine planktonic diatoms within sand beds.

5.2. Evidence for sudden, widespread, and lasting uplift

Our diatom results show sudden, widespread, and lasting RSL fall, which we infer is caused by coseismic uplift, associated with deposition of five of the six tsunami sands. These inferences are consistent with previous paleoseismic studies that used diatoms to support lithologic inferences of coseismic uplift (e.g., Sawai, 2001; Shennan et al., 2009; Briggs et al., 2014). However, unlike most previous studies, we observed no major change in lithology coincident with diatom evidence for uplift. We found minimal variation in the grain size and organic content (<20% variation) of units under- and overlying the tsunami-deposited sand beds (Figs. 6 and 7). This result is consistent with studies of modern clastic-dominated marshes that display less than a 25% difference in LOI and little change in lithology between the low and high marsh (Horton, 1999; Hawkes et al., 2010). Therefore, sudden uplift causing a shift from a low-marsh to a high-marsh environment would not necessarily result in a noticeable change in grain size or organic content, but might be evident in diatom assemblages due to reduced tidal inundation.

We observed an increase in siliceous freshwater microfossils in units overlying beds F, E, C, B, and A (Figs. 12a and 13a), suggesting a fall in RSL consistent with coseismic uplift. DCA results support our qualitative interpretations of sudden changes in diatom species

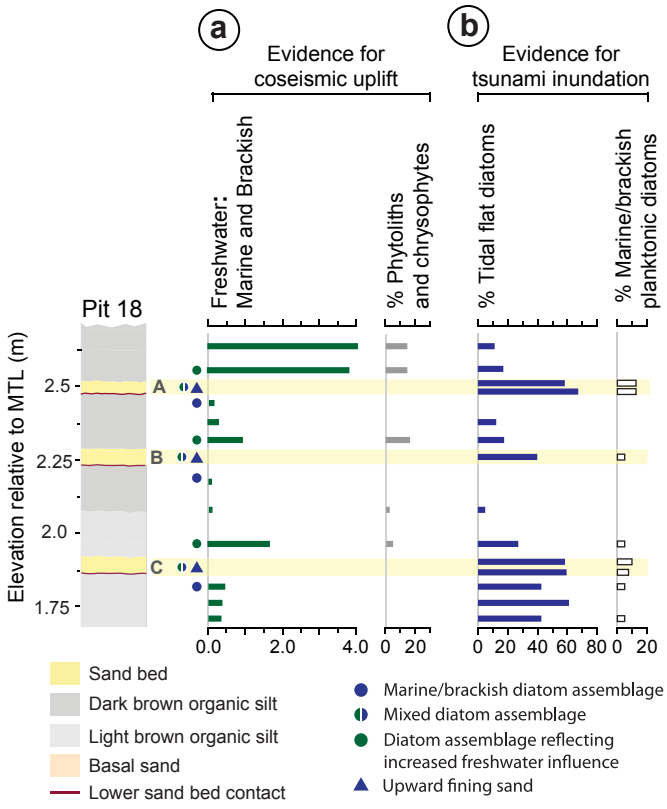

Fig. 13. Summary of evidence for coseismic uplift and tsunami inundation for pit 18. Symbols showing the nature of diatom assemblages and upward fining sequences correspond to the schematic drawing in Fig. 2. a) The summary of evidence for coseismic uplift highlights the increase in the ratio of freshwater to marine and brackish diatoms above sand beds as well as the increase in grass phytoliths and chrysophyte cysts above the sand beds. The microfossil content of the sands is left out to highlight the in assemblages across the beds. b) Evidence for tsunami inundation includes the high relative abundance of tidal flat diatoms within sand beds and the presence of marine planktonic diatoms within sand beds.

composition (Fig. 10a, b). Units underlying the sand beds generally contain diverse marine and brackish diatom assemblages dominated by tidal flat epiphytes (*A. brevipes*, *T. fasciculata*, *C. scutellum*) and/or brackish species such as the epipelic *A. coffeaeformis* and *D. smithii*, common in shallow estuarine conditions (Lepland et al., 1995; Chagué-Goff et al., 2002). Units overlying sand beds display an increase in aerophilic freshwater epiphytic diatoms (e.g., *R. gibberula*, *D. elegans*, and *G. parvulum*) and grass phytoliths and chrysophyte cysts indicating fresher, drier conditions with increased density of vegetation (e.g., Rühland et al., 2000, Fig. 10a, b). Above bed D, there is an increase in both freshwater and marine species and a slight decrease in grass phytoliths and chrysophyte cysts. Thus the evidence for uplift across this contact is equivocal.

The diatom assemblages in organic units overlying sand beds display a lasting shift in paleoecology, rather than a temporary response to short-term sea-level fluctuations (e.g., El Niño events; Witter et al., 2001) or freshwater inundation of the lowland (Hemphill-Haley, 1995a). The influx of freshwater species in the units overlying sand beds is followed by a gradual return to brackish conditions (e.g., increases in *A. coffeaeformis* below bed D and increases in *D. smithii* below beds B and A) and a decrease in freshwater species, suggesting an RSL rise, and hence interseismic land-level fall (Figs. 8 and 9).

On the basis of shifts in diatom assemblages in lowland units under- and overlying sand beds, we estimate the amount of coseismic uplift across each contact. Our estimates are only semi-quantitative because of the lack of suitable modern analog diatom data from tidal environments in central Chile. We use the modern tidal range at Quintero and the typical position within the tidal frame in which our diatom species are found to make the estimates (e.g., Nelson et al., 1995; Hemphill-Haley, 1995a; Witter et al., 2003). For example, coincident with the deposition of beds F and C, diatoms indicate a shift from a tidal flat positioned below MTL to a low marsh positioned between mean lower high water (MLHW) and mean higher high water (MHHW). At Quintero, MLHW is 0.3 m MTL and MHHW is 0.6 m MTL, indicating a fall in RSL of at least 0.3 m. Coincident with the deposition of bed E, diatoms reflect a shift from a low marsh to a high marsh positioned between MHHW and highest astronomical tide (HAT, 1.1 m MTL), indicating a fall in RSL ranging from a minimum of 0.1 m to a maximum of 0.8 m. Coincident with the deposition of beds B and A, diatoms indicate a shift from a brackish lagoon positioned between MLHW and MHHW and a freshwater marsh positioned at or near HAT, indicating a fall in RSL of at least 0.5 m.

Our identification of multiple RSL falls, which we infer were caused by coseismic uplift, coincident with deposition of sand beds strengthens our argument for their deposition by high tsunamis accompanying large, subduction-zone earthquakes. Although high storm surges with barrier breaches can produce widespread sand beds with some characteristics similar to tsunami deposits, breach deposits are not coincident with coseismic uplift (Witter et al., 2001; Morton et al., 2007; Switzer and Jones, 2008; Williams, 2009). Any reconfiguration of lowland geomorphology during storm wave erosion, such as widening of an outlet channel or migration of a spit, would likely increase the marine influence in units above sand beds rather than freshen them (e.g., Sawai et al., 2002). Tropical cyclone storm surges capable of transporting large amounts of sediment during a single storm are unprecedented in Chile (Fedorov et al., 2010).

5.3. Relative sea level and the limits to preservation of earthquake and tsunami evidence

The ~6200–3600 cal yr BP record of earthquakes and tsunamis at Quintero coincides with a period of gradual RSL rise shown in ICE-5G VM5a model predictions between ~8000 and ~4000 yrs BP (e.g., Mitrovica and Milne, 2002; Peltier, 2004; Milne et al., 2005). During this period, the eustatic contribution to sea level was dominant and net sea-level rise created a tidal flat and tidal marsh environment in the Quintero lowland that provided the accommodation space necessary to preserve earthquake and tsunami evidence (e.g., Dura et al., 2011; Brill et al., 2014). The ICE-5G VM5a model suggests this RSL rise culminated in a highstand of ~1.4 m at ~4200 cal yr BP (Peltier and Drummond, 2008). Such modeling is consistent with coastal records from central Chile that suggest an RSL highstand of at least 2 m between 6500 and 4000 cal yr BP (Ota et al., 1995; Villa-Martínez and Villagrán, 1997; Encinas et al., 2006; Saillard et al., 2009).

We found no widespread stratigraphic evidence of historical earthquakes or tsunamis in the younger, sandier, seaward sections the Quintero lowland (Fig. 5b). Even the AD 1730 tsunami, which recent models suggest exceeded 6 m in areas within 500 m of the Quintero coast (SHOA model, 2012), left no compelling sedimentary evidence (Lomnitz, 2004). We attribute the scarce evidence elsewhere along the coast to the net emergence of the central Chile coast during the late Holocene. Net Holocene emergence limits the accommodation space necessary for the preservation of earthquake and tsunami evidence resulting in brief or fragmentary paleoseismic records in Chile (e.g., Atwater et al., 1992; Nelson et al., 2009) and Sumatra (e.g., Dura et al., 2011; Grand Pre et al., 2012). For example, Nelson et al. (2009) documented stratigraphic

evidence of subsidence in the Valdivia estuary (39.5°S) from the AD 1960 earthquake, but found that a distinct unconformity separated evidence of this event from two previous subsidence events dated to ~1500 and 2300 cal yr BP. Nelson et al. (2009) attributed the fragmentary record of earthquake evidence at Valdivia to erosion and mixing of late Holocene sediments during net Holocene emergence. In contrast, paleoseismic studies conducted at Cascadia and Alaska, where a combination of tectonic, isostatic, and eustatic sea-level changes has resulted in net Holocene RSL rise with ample accommodation space, document a much more continuous stratigraphic record of coseismic subsidence over as much as 6000 years (Nelson et al., 2008, Fig. 16; e.g., Kelsey et al., 2002; Witter et al., 2003; Shennan et al., 2009).

5.4. A 500-year-interval between great earthquakes provides context for the historic earthquake record

The recurrence interval of prehistoric earthquakes and tsunamis at Quintero is comparable to recurrence intervals at other subduction zones thought to preserve evidence of only unusually large (>M_w 8.5) earthquakes and tsunamis. Between 6200 and 3600 yr BP, the interval between great subduction-zone earthquakes at Quintero ranged from ~200 to ~650 years with an average recurrence interval of ~500 years (Fig. 11). Similar recurrence intervals have been found for great earthquakes at Cascadia (e.g., Witter et al., 2003; Nelson et al., 2006), northern Japan (e.g., Sawai et al., 2009), and south central Chile (e.g., Cisternas et al., 2005; Moernaut et al., 2014). The recurrence interval for the three most recent historical earthquakes (AD 1822, 1906, and 1985) in central Chile is much shorter (~80 years) suggesting that the events recorded in the Quintero lowland were unlike those of the historical record.

In the mid-Holocene, when GIA models indicate sea level at Quintero was at least 1.4 m higher, it is possible that the lowland was in a position to record uplift from earthquakes comparable to historical events. The <1 m of uplift that characterizes the most recent historical ruptures is consistent with the range of uplift preserved in the Quintero sequence. But the low tsunamis (<4 m) produced by the AD 1822, 1906, and 1985 earthquakes are inconsistent with the distinctive sand beds we discovered in the Quintero lowland. A better historical analog for our prehistoric earthquakes and tsunamis may be the unusually large AD 1730 earthquake and high tsunami. Uplift estimates for the 1730 earthquake are unknown, but based on the comparable 1960 and 2010 earthquakes in south-central Chile, uplift associated with unusually large earthquakes is variable (0–2 m; Plafker and Savage, 1970). Thus, we interpret the record of coastal uplift and distinctive, widespread sand beds at Quintero as an archive of AD 1730-style earthquakes and tsunamis.

6. Conclusions

We used stratigraphy, lithology, diatom micropaleontology and radiocarbon dating to identify six instances of tsunami inundation at Quintero between 6200 and 3600 cal yrs BP, five of which were coincident with coastal uplift. Widespread anomalous sand beds display physical characteristics and diatom assemblages indicative of an oceanward source and high-energy deposition. The coincidence of uplift with sand deposition for five of the six sand beds is consistent with a tsunamigenic earthquake as the source for the sand. In the absence of lithologic changes across units above and below the sand beds, an abrupt increase in siliceous freshwater microfossils in units immediately overlying sand beds reveals a sudden fall in RSL coincident with tsunami deposition. The coincidence of uplift with sand deposition helps rule out storm surges and localized coastal processes as mechanisms for sand bed deposition. Paleoecological changes spanning sand beds are laterally continuous over hundreds of meters, indicating large portions of the lowland were affected, ruling out gradual RSL change and estuarine reconfiguration as mechanisms for paleoecological changes coincident with sand deposition. A significant and sustained increase in freshwater influence was observed in units overlying sand beds, followed by a gradual return to brackish and marine conditions, consistent with coseismic uplift and subsequent interseismic subsidence. Evidence of interseismic subsidence helps rule out gradual emergence of the lowland as a mechanism for paleoecological changes coincident with sand deposition. We infer <1 m of uplift during five of the six earthquakes based on present-day tidal datums and changes in diatom assemblages in units above and below sand beds.

Our interpretations have important implications for evaluating earthquake hazards in central Chile. Basing hazard assessments on only the most recent, well-documented, but smaller earthquakes and tsunamis in 1822, 1906, and 1985, overlooks the higher hazard posed by larger earthquakes and higher tsunamis, such as those which occurred in 1730 and hundreds of years apart between 6200 and 3600 cal yr BP. The recent experience of underestimating the potential of the Sumatra and Japan megathrusts to produce unusually large earthquakes (Jankaew et al., 2008; Sawai et al., 2012)—based on only a limited historical record—emphasizes the importance of using the prehistoric record in estimating the hazard to which the current coastal population is exposed. Comprehensive earthquake hazard assessments in central Chile should consider the effects of the largest earthquakes and tsunamis that have repeatedly struck this coast.

Acknowledgments

This work was supported by Chile's Fondo Nacional de Desarrollo Científico y Tecnológico (FONDECYT N° 1110848 to MC) and the National Science Foundation (grant EAR-1144537 and 1145170). Nelson is supported by the Earthquake Hazards Program of the U.S. Geological Survey. We are grateful to Brian Atwater, Catherine Chagúe-Goff, James Goff, Marcelo Lagos, Diego Muñoz, and Yuki Sawai for support during fieldwork, Daniel Melnick for providing elevation data, Lorena Rebolledo for her preliminary diatom analyses, and Sonja Hausmann and Don Charles at the Academy of Natural Sciences in Philadelphia, USA, for their assistance with diatom analyses. We thank Harvey Kelsey, Brian Sherrod, and Simon Engelhart for constructive reviews that substantially improved the manuscript. Any use of trade, product, or firm names is for descriptive purposes only and does not imply endorsement by the U.S. Government. This paper is a contribution to IGCP project 588 'Preparing for coastal change'.

References

Allen, J.R.L., 2000. Morphodynamics of Holocene salt marshes: a review sketch from the Atlantic and Southern North Sea coasts of Europe. Quat. Sci. Rev. 19, 1155–1231.

Arcos, M.E.M., 2012. A Holocene sedimentary record of tectonically influenced reduced channel mobility, Skokomish River delta, Washington State, USA. Geomorphology 177, 93–107.

Atwater, B.F., 1987. Evidence for great earthquakes along the outer coast of Washington State. Science 236, 942–944. http://dx.doi.org/10.1126/science.236.4804.942.

Atwater, B.F., Nunez, H.J., Vita-Finzi, C., 1992. Net late Holocene emergence despite earthquake-induced submergence, south-central Chile. In: Ota, Y., Nelson, A.R., Berryman, K.R. (Eds.), Impacts of Tectonics on Quaternary Coastal Evolution, Quaternary International, vol. 15/16. Pergamon, Oxford, pp. 77–85.

Atwater, B.F., Hemphill-Haley, E., 1997. Recurrence Intervals for Great Earthquakes of the Past 3,500 Years at Northeastern Willapa Bay, pp. 1–108. Washington. U.S. Geological Survey Professional Paper, (1576).

Ball, D.F., 1964. Loss-on-ignition as an estimate of organic matter and organic carbon in non-calcareous soils. J. Soil Sci. 15, 84–92.
Barrientos, S.E., 1995. Dual seismogenic behavior: the 1985 Central Chile earthquake. Geophys. Res. Lett. 22 (24), 3541–3544.
Barrientos, S.E., 1996. On Predicting Coastal Uplift and Subsidence Due to Large Earthquakes in Chile. Third ISAG, ORSTOM, St Malo, France, pp. 145–148.
Barrientos, S.E., 1997. Central Chile: an example of quasi-static crustal behavior. Isl. Arc 6, 281–287.
Barrientos, S.E., 2007. Earthquakes in Chile. In: Moreno, T., Gibbons, W. (Eds.), Geology of Chile. The Geological Society, London, pp. 263–287.
Bartsch-Winkler, S., Schmoll, H., 1993. Evidence for late Holocene relative sea-level fall from reconnaissance stratigraphical studies in an area of earthquake-subsided intertidal deposits, Isla Chiloe, southern Chile. In: Frostwick, L.E., Steel, R.J. (Eds.), Tectonic Controls and Signatures in Sedimentary Successions. International Association of Seismologists, pp. 91–108.
Beck, S., Barrientos, S.E., Kausel, E., Reyes, M., 1998. Source characteristics of historical earthquakes along central Chile subduction zone. J. South Am. Earth Sci. 11, 115–129.
Berryman, K., Cooper, A., Norris, R., Villamor, P., Sutherland, R., Wright, T., Schermer, E., Langridge, R., Biasi, G., 2012. Late Holocene rupture history of the Alpine fault in South Westland, New Zealand. Bull. Seismol. Soc. Am. 102 (2), 620–638. http://dx.doi.org/10.1785/0120110177.
Briggs, R.W., Engelhart, S.E., Nelson, A.R., Dura, T., Kemp, A.C., Haeussler, P.J., Corbett, D.R., Angster, S.J., Bradley, L.A., 2014. Uplift and subsidence reveal a non-persistent megathrust rupture boundary (Sitkinak Island, Alaska). Geophys. Res. Lett. 41 (7), 2289–2296.
Brill, D., Jankaew, K., Neubauer, N.P., Kelletat, D., Scheffers, A., Vött, A., Brückner, H., 2014. Holocene coastal evolution of southwest Thailand—implications for the site-specific preservation of palaeotsunami deposits. Z. Geomorphol. 58 (1).
Bronk Ramsey, C., 2008. Depositional models for chronological records. Quat. Sci. Rev. 27 (1–2), 42–60. http://dx.doi.org/10.1016/j.quascirev.2007.01.019.
Bronk Ramsey, C., 2009. Bayesian analysis of radiocarbon ages. Radiocarbon 51 (1), 337–360.
Caviedes, C., 1972. Geomorfologia del Cuaternario del Valle del Aconcagua, Chile central. Friebg. Geogr. Hefte 11, 153.
Chagué-Goff, C., Dawson, S., Goff, J.R., Zachariasen, J., Berryman, K.R., Garnett, D.L., Waldron, H.M., Mildenhall, D.C., 2002. A tsunami (ca. 6300 years BP) and other Holocene environmental changes, northern Hawke's Bay, New Zealand. Sediment. Geol. 150 (1), 89–102.
Charles, D., 2002. Protocols for the Analysis of Algal Samples Collected as Part of the U.S. Geological Survey National Water-quality Assessment Program. Patrick Center for Environmental Research, Philadelphia. Academy of Natural Sciences.
Cisternas, M., 2012. El terremoto de 1647 de Chile central como un evento intraplaca: ¿otra amenaza para Chile metropolitano? Rev. Geogr. Norte Gd. 53, 23–33.
Cisternas, M., Atwater, B.F., Torrejón, F., Sawai, Y., Machuca, G., Lagos, M., Husni, M., 2005. Predecessors of the giant 1960 Chile earthquake. Nature 437 (7057), 404–407.
Cisternas, M., Torrejón, F., Gorigoitia, N., 2012. Amending and complicating Chile's seismic catalog with the Santiago earthquake of 7 August 1580. J. South Am. Earth Sci. 33 (1), 102–109.
Combellick, R.A., Reger, R.D., 1994. Sedimentological and Radiocarbon-age Data for Tidal Marshes along Eastern and Upper Cook Inlet, Alaska. Department of Natural Resources, Division of Geological and Geophysical Surveys, State of Alaska.
Comte, D., Eisemberg, A., Lorca, E., Pardo, M., Ponce, L., Saragoni, R., Singh, S.K., Suárez, G., 1986. The 1985 central Chile earthquake: a repeat of previous great earthquakes in the region? Science 233, 449–453.
Dawson, S., 2007. Diatom biostratigraphy of tsunami deposits: examples from the 1998 Papua New Guinea tsunami. Sediment. Geol. 200, 328–335.
Darienzo, M.E., Peterson, C.D., Clough, C., 1994. Stratigraphic evidence for great subduction zone earthquakes at four estuaries in northern Oregon, USA. J. Coast. Res. 10, 850–876.
Denys, L., 1991. A Check-list of the Diatoms in the Holocene Deposits of the Western Belgian Coastal Plain with a Survey of Their Apparent Ecological Requirements. Ministère des affaires économiques, Service Géologique de Belgique.
Donato, S.V., Reinhardt, E.G., Boyce, J.I., Pilarczyk, J.E., Jupp, B.P., 2009. Particle-size distribution of inferred tsunami deposits in Sur Lagoon, Sultanate of Oman. Mar. Geol. 257, 54–64.
Dura, T., Rubin, C.M., Kelsey, H.M., Horton, B.P., Hawkes, A., Vane, C.H., Daryono, M., Grand Pre, C., Ladinsky, T., Bradley, S., 2011. Stratigraphic record of Holocene coseismic subsidence, Padang, West Sumatra. J. Geophys. Res. Solid Earth 116 (B11).
DuRoss, C.B., Personius, S.F., Crone, A.J., Olig, S.S., Lund, W.R., 2011. Integration of paleoseismic data from multiple sites to develop an objective earthquake chronology: application to the Weber segment of the Wasatch fault zone, Utah. Bull. Seismol. Soc. Am. 101 (6), 2765–2781. http://dx.doi.org/10.1785/0120110102.
Ely, L.L., Cisternas, M., Wesson, R.L., Dura, T., 2014. Five centuries of tsunamis and land-level changes in the overlapping rupture area of the 1960 and 2010 Chilean earthquakesm. Geology. G35830-1.
Encinas, A., Herve, F., Villa Martinez, R., Nielsen, S., Finger, K., Peterson, D., 2006. Finding of a Holocene marine layer in Algarrobo (33°22'S), central Chile. Implic. Coast. Uplift Rev. Geol. Chile 33 (2), 339–345.
Fedorov, A.V., Brierley, C.M., Emanuel, K., 2010. Tropical cyclones and permanent El Niño in the early Pliocene epoch. Nature 463 (7284), 1066–1070.
Garrett, E., Shennan, I., Watcham, E.P., Woodroffe, S.A., 2013. Reconstructing paleoseismic deformation, 1: modern analogues from the 1960 and 2010 Chilean great earthquakes. Quat. Sci. Rev. 75 (0), 11–21. http://dx.doi.org/10.1016/j.quascirev.2013.04.007.
Gelfenbaum, G., Jaffe, B., 2003. Erosion and sedimentation from the 17 July 1998 Papua New Guinea tsunami. Pure Appl. Geophys. 160, 1969–1999.
Geller, R.J., 2011. Shake-up time for Japanese seismology. Nature 472 (7344), 407–409. http://dx.doi.org/10.1038/nature10105.
Goff, J., Chagué-Goff, C., Nichol, S., Jaffe, B., Dominey-Howes, D., 2012. Progress in palaeotsunami research. Sediment. Geol. 243, 70–88.
Goto, K., Chagué-Goff, C., Fujino, S., Goff, J., Jaffe, B., Nishimura, Y., Richmond, B., Sugawara, D., Szczuciński, W., Tappin, D.R., Witter, R., Yulianto, E., 2011. New insights of tsunami hazard from the 2011 Tohoku-oki event. Mar. Geol. 290, 46–50.
Grand Pre, C.A., Horton, B.P., Kelsey, H.M., Rubin, C.M., Hawkes, A.D., Daryono, M.R., Rosenberg, G., Culver, S.J., 2012. Stratigraphic evidence for an early Holocene earthquake in Aceh, Indonesia. Quat. Sci. Rev. 54, 142–151.
Hamilton, S., Shennan, I., Combellick, R., Mulholland, J., Noble, C., 2005. Evidence for two great earthquakes at Anchorage, Alaska and implications for multiple great earthquakes through the Holocene. Quat. Sci. Rev. 24 (18), 2050–2068.
Hartley, B., Ross, R., Williams, D.M., 1986. A check-list of the freshwater, brackish and marine diatoms of the British Isles and adjoining coastal waters. J. Mar. Biol. Assoc. U. K. 66 (03), 531–610.
Hawkes, A.D., Bird, M., Cowie, S., Grundy-Warr, C., Horton, B.P., Shau Hwai, A.T., Aik, L.W., 2007. Sediments deposited by the 2004 Indian Ocean tsunami along the Malaysia–Thailand Peninsula. Mar. Geol. 242 (1), 169–190.
Hawkes, A.D., Horton, B.P., Nelson, A.R., Vane, C.H., Sawai, Y., 2010. The application of intertidal foraminifera to reconstruct coastal subsidence during the giant Cascadia earthquake of AD 1700 in Oregon, USA. Quat. Int. 122, 116–140.
Heki, K., 2011. A tale of two earthquakes. Science 332 (6036), 1390–1391. http://dx.doi.org/10.1126/science.1206643.
Hemphill-Haley, E., 1995. Diatom evidence for earthquake-induced subsidence and tsunami 300 years ago in southern coastal Washington. Geol. Soc. Am. Bull. 107, 367–378.
Hemphill-Haley, E., 1996. Diatoms as an aid in identifying late-Holocene tsunami deposits. Holocene 6 (4), 439–448.
Hogg, A.G., Hua, Q., Blackwell, P.G., Niu, M., Buck, C.E., Guilderson, T.P., Heaton, T.J., 2013. SHCAL13 Southern Hemisphere calibration, 0-50,000 Years Cal BP. Radiocarbon 55 (4).
Horton, B.P., 1999. The distribution of contemporary intertidal foraminifera at Cowpen Marsh, Tees Estuary, UK: implications for studies of Holocene sea-level changes. Palaeogeogr. Palaeoclimatol. Palaeoecol. 149 (1), 127–149.
Horton, B.P., Edwards, B.P., 2006. Quantifying Holocene sea-level change using intertidal foraminifera: lessons from the British Isles. Cushman Found. Foraminifer. Res. 40, 97. Special Publication.
Horton, B.P., Sawai, Y., Hawkes, A.D., Witter, R.C., 2011. Sedimentology and paleontology of a tsunami deposit accompanying the great Chilean earthquake of February 2010. Mar. Micropaleontol. 79, 132–138.
Jaffe, B., Buckley, M., Richmond, B., Strotz, L., Etienne, S., Clark, K., Watt, S., Gelfenbaum, G., Goff, J., 2011. Flow speed estimated by inverse modeling of sandy sediment deposited by the 29 September 2009 tsunami near Satitoa, east Upolu, Samoa. Earth-Sci. Rev. 107, 23–37.
Jankaew, K., Atwater, B., Sawai, Y., Choowong, M., Charoentitirat, T., Martin, M., Prendergast, A., 2008. Medieval forewarning of the 2004 Indian Ocean tsunami in Thailand. Nature 455, 1228–1231.
Kelsey, H.M., Witter, R.C., Hemphill-Haley, E., 2002. Plate-boundary earthquakes and tsunamis of the past 5500 yr, Sixes River estuary, southern Oregon. Geol. Soc. Am. Bull. 114 (3), 298–314.
Kelleher, J., 1972. Rupture zones of large South American earthquakes and some predictions. J. Geophys. Res. 77, 2087–2103.
Kemp, A.C., Nelson, A.R., Horton, B.P., 2013. Radiocarbon dating of plant macrofossils from tidal-marsh sediment. In: Shroder, John F. (Ed.), Treatise on Geomorphology, vol. 14. Academic Press, San Diego, pp. 370–388.
Krammer, K., Lange-Bertalot, H., 1986. Bacillariophyceae 2/1. Naviculaceae. In: Ettl, H., Gerloff, J., Heynig, H., Mollenhauser (Eds.), Süsswasserflora von Mitteleuropa. Gustav Fischer Verlag, Stuttgart, pp. 1–876.
Krammer, K., Lange-Bertalot, H., 1988. Bacillariophyceae 2/2. Basillariaceae, Epithemiaceae, Surirellaceae. In: Ettl, H., Gerloff, J., Heynig, H., Mollenhauser (Eds.), Süsswasserflora von Mitteleuropa. Gustav Fischer Verlag, Stuttgart, pp. 1–600.
Krammer, K., Lange-Bertalot, H., 1991a. Bacillariophyceae 2/3. Centrales, Fragilariaceae, Eunotiaceae. In: Ettl, H., Gerloff, J., Heynig, H., Mollenhauser (Eds.), Süsswasserflora von Mitteleuropa. Gustav Fischer Verlag, Stuttgart, pp. 1–600.
Krammer, K., Lange-Bertalot, H., 1991b. Bacillariophyceae 2/4. Achnanthaceae, Kritische Erganzungen zu Navicula (Lineolatae) und Gomphonema. In: Ettl, H. (Ed.), Pascher's Süsswasserflora von Mitteleuropa, vol. 2, part 4. Gustav Fischer Verlag, Stuttgart, pp. 1–437.
Lange-Bertalot, H., 2000. In: Lange-Bertalot, H. (Ed.), Iconographia Diatomologica Annotated Diatom Micrographs – Diatom Flora of Marine Coasts I, vol. 7. Koeltz Scientific Books. Copyright: A.R.G. Gantner Verlag K.G. By: Andrzej Witkowiski, Horst Lange- Bertalot and Ditmar Metzeltin.
Lepland, A., Miller, U., Sakson, M., 1995. Palaeoenvironmental conditions during the Baltic Yoldia stage in the Tallinn area, northern Estonia. Quat. Int. 27, 83–94.

Lu, H., Liu, K., 2003. Phytoliths of common grasses in the coastal environments of southeastern USA. Estuarine, Coast. and Shelf Sci. 58 (3), 587–600.

Lomnitz, C., 1970. Major earthquakes and tsunamis in Chile during the period 1535 to 1955. Int. J. Earth Sci. 59, 938–960.

Lomnitz, C., 2004. Major earthquakes of Chile: a historical survey, 1535-1960. Seismol. Res. Lett. 75 (3), 368–378.

Maldonado, A., Villagrán, C., 2006. Climate variability over the last 9900 cal yr BP from a swamp forest pollen record along the semiarid coast of Chile. Quat. Res. 66 (2), 246–258. http://dx.doi.org/10.1016/j.yqres.2006.04.003.

Martínez, C., Quezada, M., Rubio, P., 2011. Historical changes in the shoreline and littoral processes on a headland bay beach in central Chile. Geomorphology 135 (1), 80–96.

May, S.M., Pint, A., Rixhon, G., Kelletat, D., Wennrich, V., Brückner, H., 2013. Holocene coastal stratigraphy, coastal changes and potential palaeoseismological implications inferred from geo-archives in Central Chile (29–32° S). Z. für Geomorphol. Suppl. Issues 57 (4), 201–228.

Melnick, D., Bookhagen, B., Strecker, M.R., Echtler, H.P., 2009. Segmentation of megathrust rupture zones from fore-arc deformation patterns over hundreds to millions of years, Arauco peninsula, Chile. J. Geophys. Res.: Solid Earth 114 (B1).

Métois, M., Socquet, A., Vigny, C., 2012. Interseismic coupling, segmentation and mechanical behavior of the central Chile subduction zone. J. Geophys. Res. Solid Earth 117 (B3), B03406. http://dx.doi.org/10.1029/2011JB008736.

Mitrovica, J., Milne, G., 2002. On the origin of late Holocene sea-level highstands within equatorial ocean basins. Quat. Sci. Rev. 21 (20–22), 2179–2190. http://dx.doi.org/10.1016/S0277-3791(02)00080-X.

Milne, G.A., Long, A.J., Bassett, S.E., 2005. Modeling Holocene relative sea-level observations from the Caribbean and South America. Quat. Sci. Rev. 24 (10–11), 1183–1202. http://dx.doi.org/10.1016/j.quascirev. 2004.10.005.

Moernaut, J., De Batist, M., Heirman, K., Van Daele, M., Pino, M., Brümmer, R., Urrutia, R., 2009. Fluidization of buried mass-wasting deposits in lake sediments and its relevance for paleoseismology: results from a reflection seismic study of lakes Villarrica and Calafquén (South-Central Chile). Sediment. Geol. 213 (3), 121–135.

Moernaut, J., Daele, M.V., Heirman, K., Fontijn, K., Strasser, M., Pino, M., De Batist, M., 2014. Lacustrine turbidites as a tool for quantitative earthquake reconstruction: new evidence for a variable rupture mode in south central Chile. J. Geophys. Res. Solid Earth 119 (3), 1607–1633.

Monecke, K., Finger, W., Klarer, D., Kongko, W., McAdoo, B., Moore, A., Sudrajat, S., 2008. A 1,000 year sediment record of tsunami recurrence in northern Sumatra. Nature 455, 1232–1234.

Moreno, T., Gibbons, W. (Eds.), 2007. The Geology of Chile. The Geological Society of London, pp. 21–114.

Morton, R.A., Gelfenbaum, G., Jaffe, B.E., 2007. Physical criteria for distinguishing sandy tsunami and storm deposits using modern examples. Sediment. Geol. 200, 184–207.

Munsell soil color charts, 1975. Macbeth division of Kollmorgen Corporation.

Nelson, A.R., Atwater, B.F., Bobrowsky, P.T., Bradley, L., Clague, J.J., Carver, G.A., Darienzo, M.E., 1995. Radiocarbon evidence for extensive plate-boundary rupture about 300 years ago at the Cascadia subduction zone. Nature 378, 371–374.

Nelson, A.R., Shennan, I., Long, A.J., 1996. Identifying coseismic subsidence in tidal-wetland stratigraphic sequences at the Cascadia subduction zone of western North America. J. Geophys. Res. 101, 6115–6135.

Nelson, A.R., Ota, Y., Umitsu, M., Kashima, K., Matsushima, Y., 1998. Seismic or hydrodynamic control of rapid late-Holocene sea-level rises in southern coastal Oregon, USA? Holocene 8 (3), 287–299.

Nelson, A.R., Kelsey, H.M., Witter, R.C., 2006. Great earthquakes of variable magnitude at the Cascadia subduction zone. Quat. Res. 65 (3), 354–365.

Nelson, A.R., Sawai, Y., Jennings, A.E., Bradley, L.A., Gerson, L., Sherrod, B.L., Sabean, J., Horton, B.P., 2008. Great-earthquake paleogeodesy and tsunamis of the past 2000 years at Alsea Bay, central Oregon coast, USA. Quat. Sci. Rev. 27 (7), 747–768.

Nelson, A.R., Kashima, K., Bradley, L., 2009. Fragmentary evidence of great-earthquake subsidence during Holocene emergence, Valdivia Estuary, south central Chile. Bull. Seismol. Soc. Am. 99 (1), 71–86.

Ota, Y., Miyauchi, T., Paskoff, R., Koba, M., 1995. Plio-Quaternary marine terraces and their deformation along the Altos de Talinay, north-central Chile. Andean Geol. 22 (1), 89–102.

Ovenshine, A.T., Lawson, D.E., 1976. The Placer River Silt–An Intertidal Deposit Caused by the 1964 Alaska Earthquake.

Pardo, M., Comte, D., Monfret, T., 2002. Seismotectonic and stress distribution in the central Chile subduction zone. Flat-Slab Subduction Andes 15 (1), 11–22. http://dx.doi.org/10.1016/S0895-9811(02)00003-2.

Peltier, W.R., 2004. Global glacial isostasy and the surface of the ice-age Earth: the ICE-5G (VM2) model and GRACE. Annu. Rev. Earth Planet. Sci. 32, 111–149.

Peltier, W.R., Drummond, R., 2008. Rheological stratification of the lithosphere: a direct inference based upon the geodetically observed pattern of the glacial isostatic adjustment of the North American continent. Geophys. Res. Lett. 35 http://dx.doi.org/10.1029/2008GL034586.

Plafker, G., Savage, J.C., 1970. Mechanism of the Chilean earthquakes of May 21 and 22, 1960. Geol. Soc. Am. Bull. 81, 1001–1030.

Plafker, G., Lajoie, K.R., Rubin, M., 1992. Determining recurrence intervals of great subduction zone earthquakes in southern Alaska by radiocarbon dating. In: Radiocarbon After Four Decades. Springer, New York, pp. 436–453.

Rebolledo, L., Lange, C.B., Figueroa, D., Pantoja, S., Muñoz, P., Castro, R., 2005. 20th century fluctuations in the abundance of siliceous microorganisms preserved in the sediments of the Puyuhuapi channel (44 S), Chile. Rev. Chil. Hist. Nat. 78, 469–488.

Rebolledo, L., González, H.E., Muñoz, P., Iriarte, J.L., Lange, C.B., Pantoja, S., Salamanca, M., 2011. Siliceous productivity changes in Gulf of Ancud sediments (42° S, 72° W), southern Chile, over the last~ 150 years. Cont. Shelf Res. 31 (3), 356–365.

Rhodes, B., Tuttle, M., Horton, B.P., Doner, L., Kelsey, H.M., Nelson, A., Cisternas, M., 2006. Paleotsunami research. Eos, Trans. Am. Geophys. Union 87 (21), 205–209.

Rivera, R., 2000. Guide for References and Distribution for the Class Bacillariophyceae in Chile between 18°28'S and 58°S. J. Cramer.

Ruegg, J.C., Rudloff, A., Vigny, C., Madariaga, R., De Chabalier, J.B., Campos, J., Dimitrov, D., 2009. Interseismic strain accumulation measured by GPS in the seismic gap between Constitución and Concepción in Chile. Phys. Earth Planet. Inter. 175 (1), 78–85.

Rühland, K., Smol, J.P., Jasinski, J.P.P., Warner, B., 2000. Response of diatoms and other siliceous indicators to the developmental history of a peatland in the Tiksi Forest, Siberia, Russia. Arct. Antarct. Alp. Res. 32, 167–178.

Saillard, M., Hall, S.R., Audin, L., Farber, D.L., Hérail, G., Martinod, J., Bondoux, F., 2009. Non-steady long-term uplift rates and Pleistocene marine terrace development along the Andean margin of Chile (31° S) inferred from ^{10}Be dating. Earth Planet. Sci. Lett. 277 (1), 50–63.

Sambridge, M., Braun, J., McQueen, H., 1995. Geophysical parametrization and interpolation of irregular data using natural neighbors. Geophys. J. Int. 122, 837–857.

Satake, K., Atwater, B.F., 2007. Long-term perspectives on giant earthquakes and tsunamis at subduction zones. Annu. Rev. Earth Planet. Sci. 35, 349–374.

Sawai, Y., 2001. Episodic emergence in the past 3000 years at the Akkeshi Estuary, Hokkaido, northern Japan. Quat. Res. 56, 231–241.

Sawai, Y., Nasu, H., Yasuda, Y., 2002. Fluctuations in relative sea-level during the past 3000 yr in the Onnetoh Estuary, Hokkaido, northern Japan. J. Quat. Sci. 17, 607–622.

Sawai, Y., Fujii, Y., Fujiwara, O., Kamataki, T., Komatsubara, J., Okamura, Y., Shishikura, M., 2008. Marine incursions of the past 1500 years and evidence of tsunamis at Suijin-numa, a coastal lake facing the Japan Trench. Holocene 18 (4), 517–528.

Sawai, Y., Jankaew, K., Martin, M.E., Prendergast, A., Choowong, M., Charoentitirat, T., 2009. Diatom assemblages in tsunami deposits associated with the 2004 Indian Ocean tsunami at Phra Thong Island, Thailand. Mar. Micropaleontol. 73, 70–79.

Sawai, Y., Namegaya, Y., Okamura, Y., Satake, K., Shishikura, M., 2012. Challenges of anticipating the 2011 Tohoku earthquake and tsunami using coastal geology. Geophys. Res. Lett. 39 (21).

Servicio Hidrográfico y Oceanográfico de la Armada (SHOA), 2011, Carta de inundacion por tsunami referida al evento del año 1730: Servicio Hidrográfico y Oceanográfico de la Armada de Chile.

Shennan, I., Scott, D.B., Rutherford, M., Zong, Y.Q., 1999. Microfossil analysis of sediments representing the 1964 earthquake, exposed at Girdwood Flats, Alaska, USA. Quat. Int. 60, 55–73.

Shennan, I., Hamilton, S., 2006. Coseismic and pre-seismic subsidence associated with great earthquakes in Alaska. Quat. Sci. Rev. 25 (1), 1–8.

Shennan, I., Bruhn, R., Plafker, G., 2009. Multi-segment earthquakes and tsunami potential of the Aleutian megathrust. Quat. Sci. Rev. 28 (1), 7–13.

Sherrod, B.L., 2001. Evidence for earthquake-induced subsidence about 1100 yr ago in coastal marshes of southern Puget Sound, Washington. Geol. Soc. Am. Bull. 113 (10), 1299–1311.

Soloviev, S.L., Go, ChN., 1984. Catalogue of Tsunamis on the eastern shore of the Pacific Ocean. In: Canadian Translation of Fisheries and Aquatic Sciences No. 5078. Canada Institute for Scientific and Technical Information, National Research Council, Ottawa, p. 293.

Stein, S., Okal, E.A., 2011. The size of the 2011 Tohoku earthquake need not have been a surprise. Eos, Trans. Am. Geophys. Union 92 (27), 227–228.

Switzer, A.D., Jones, B.G., 2008. Large-scale washover sedimentation in a freshwater lagoon from the southeast Australian coast: sea-level change, tsunami or exceptionally large storm? Holocene 18 (5), 787–803. http://dx.doi.org/10.1177/0959683608089214.

Szczuciński, W., Kokociński, M., Rzeszewski, M., Chagué-Goff, C., Cachão, M., Goto, K., Sugawara, D., 2012. Sediment sources and sedimentation processes of 2011 Tohoku-oki tsunami deposits on the Sendai Plain, Japan — insights from diatoms, nannoliths and grain size distribution. Sediment. Geol. http://dx.doi.org/10.1016/j.sedgeo.2012.07.019.

Udías, A., Madariaga, R., Buforn, E., Muñoz, D., Ros, M., 2012. The large Chilean historical earthquakes of 1647, 1657, 1730, and 1751 from contemporary documents. Bull. Seismol. Soc. Am. 102 (4), 1639–1653. http://dx.doi.org/10.1785/0120110289.

Villa-Martínez, R., Villagrán, C., 1997. Historia de La Vegetación de Bosques Pantanosos de La Costa de Chile Central Durante El Holoceno Medio Y Tardío. Rev. Chil. Hist. Nat. 70 (3), 391–401.

Vigny, C., Socquet, A., Peyrat, S., Ruegg, J.-C., Métois, M., Madariaga, R., Morvan, S., 2011. The 2010 Mw 8.8 Maule megathrust earthquake of central Chile, Monitored by GPS. Science 332 (6036), 1417–1421. http://dx.doi.org/10.1126/science.1204132.

Vos, P.C., de Wolf, H., 1988. Methodological aspects of paleo-ecological diatom research in coastal areas of the Netherlands. Neth. J. Geosci./Geol. Mijnb. 67, 31–40.

Vos, Peter C., de Wolf, H., 1993. Diatoms as a tool for reconstructing sedimentary environments in coastal wetlands; methodological aspects. In: Twelfth International Diatom Symposium. Springer, Netherlands, pp. 285–296.
Williams, H.F., 2009. Stratigraphy, sedimentology, and microfossil content of Hurricane Rita storm surge deposits in southwest Louisiana. J. Coast. Res. 1041–1051.
Williams, H.F., Hutchinson, I., Nelson, A.R., 2005. Multiple sources for late-Holocene tsunamis at Discovery Bay, Washington State, USA. Holocene 15 (1), 60–73.
Witter, R.C., Kelsey, H.M., Hemphill-Haley, E., 2001. Pacific storms, El Nino and tsunamis: competing mechanisms for sand deposition in a coastal marsh, Euchre Creek, Oregon. J. Coast. Res. 563–583.
Witter, R.C., Kelsey, H.M., Hemphill-Haley, E., 2003. Great Cascadia earthquakes and tsunamis of the past 6700 years, Coquille River estuary, southern coastal Oregon. Geol. Soc. Am. Bull. 115 (10), 1289–1306.